Western diet increases COVID-19 disease severity in the Syrian hamster

Julia R. Port[1]*, Danielle R. Adney[1]*, Benjamin Schwarz[2], Jonathan E. Schulz[1], Daniel E. Sturdevant[3], Brian J. Smith[4], Victoria A. Avanzato[1], Myndi G. Holbrook[1], Jyothi N. Purushotham[1], Kaitlin A. Stromberg[2], Ian Leighton[2], Catharine M. Bosio[2], Carl Shaia[4], Vincent J. Munster[1]#

1. Laboratory of Virology, National Institute of Allergy and Infectious Diseases, National Institutes of Health, Hamilton, MT, USA
2. Laboratory of Bacteriology, National Institute of Allergy and Infectious Diseases, National Institutes of Health, Hamilton, MT, USA
3. Genomics Unit, Research Technologies Branch, National Institute of Allergy and Infectious Diseases, National Institutes of Health, Hamilton, MT, USA
4. Rocky Mountain Veterinary Branch, Division of Intramural Research, National Institutes of Health, Hamilton, MT, USA

*These authors contributed equally

#Corresponding author: Vincent Munster, email: vincent.munster@nih.gov

Summary (150 words)

Pre-existing comorbidities such as obesity or metabolic diseases can adversely affect the clinical outcome of COVID-19. Chronic metabolic disorders are globally on the rise and often a consequence of an unhealthy diet, referred to as a Western Diet. For the first time in the Syrian hamster model, we demonstrate the detrimental impact of a continuous high-fat high-sugar diet on COVID-19 outcome. We observed increased weight loss and lung pathology, such as exudate, vasculitis, hemorrhage, fibrin, and edema, delayed viral clearance and functional lung recovery, and prolonged viral shedding. This was accompanied by an increased trend of systemic IL-10 and IL-6, as well as a dysregulated serum lipid response dominated by polyunsaturated fatty acid-containing phosphatidylethanolamine, recapitulating cytokine and lipid responses associated with severe human COVID-19. Our data support the hamster model for testing restrictive or targeted diets and immunomodulatory therapies to mediate the adverse effects of metabolic disease on COVID-19.

Keywords: Syrian hamster, SARS-CoV-2, obesity, pathogenesis, lipid metabolism

Introduction

Severe acute respiratory syndrome coronavirus-2 (SARS-CoV-2) is the etiological agent of coronavirus disease (COVID)-19 and can cause asymptomatic to severe lower respiratory tract infections in humans (Nie et al., 2020; Parry et al., 2020). Pre-existing comorbidities such as immunosuppression, obesity, diabetes, or chronic lung disease can adversely affect the clinical outcome (Butler and Barrientos, 2020; Hussain et al., 2020; Li et al., 2009; Petrakis et al., 2020). Of these, obesity and metabolic disorders are global pandemics of rising concern (Araújo et al., 2019; Saklayen, 2018; Swinburn et al., 2011). The underlying disease is driven mainly by changes in the global food system, which is producing more processed, affordable, and effectively marketed food than ever before. This diet, rich in saturated fats and refined sugars, is referred to as a Western Diet (Cordain et al., 2005). Long-term consumption of a Western Diet may result in chronic activation of the immune system, impairing both innate and adaptive responses (Green and Beck, 2017a, b; Rogero and Calder, 2018). The Western Diet has been associated with non-alcoholic steatohepatitis (NASH) and non-alcoholic fatty liver disease (NAFLD). These disease syndromes predispose individuals to multiple comorbidities that can include cirrhosis and liver failure. The relative risk of hospitalization and severe COVID-19 outcome are significantly increased for patients afflicted by these comorbidities (Butler and Barrientos, 2020). This has resulted in disproportionately worse outcomes in US ethnic and racial minorities, where prevalence and incidence of metabolic disorders are increased (Cefalu and Rodgers, 2021).

It is currently unclear how certain comorbidities may determine disease manifestation of COVID-19. Different studies have demonstrated that the Syrian hamster model is suitable to model aspects of obesity and diabetes and for studying lipid metabolism (Dalbøge et al., 2015; Kasim-Karakas et al., 1996). In healthy hamsters, SARS-CoV-2 infection is associated with mild to moderate clinical disease (Chan et al., 2020; Rosenke et al., 2020; Sia et al., 2020). However, no studies have investigated COVID-19 in hamsters with comorbidities. Here we show in a Syrian hamster model how a continuous high-fat high-sugar (HFHS) diet changed the metabolomic state

in the Syrian hamster and the resulting consequences on viral replication dynamics, immune protection and disease severity after infection with SARS-CoV-2.

Results

High-fat and high-sugar diet induces metabolic changes characterized by increased early weight gain and glucose tolerance

We investigated the impact of a consistent high-fat and high-sugar (HFHS) diet on the Syrian hamster. Either a regular rodent (RD) diet or a high-calorimetric HFHS diet was given to male Syrian hamsters (4-6 week old) for 16 weeks *ad libitum* (N = 35, respectively). Weight gain of juvenile hamsters was monitored weekly. Initially, animals on the HFHS diet gained weight faster than animals on the regular diet. Difference in median weights was significant from the 2nd week onwards until week 10 (**Fig 1 A**, N = 35, ordinary two-way ANOVA, followed by Sidak's multiple comparisons test, p = 0.001, p = <0.001, p = <0.001, p = <0.001, p = <0.001, p = <0.001, p = <0.001, p = 0.0011, p = <0.001). After week 10 weight gain either plateaued or decreased in the HFHS group (median = 165 g), while in the regular diet group weight increased until week 12 (median = 160 g), at which point the median weight between groups showed no significant difference. We observed morbidity (4/35 = 11%) in the HFHS group, which was absent in the RD group.

To assess the levels of glucose-associated symptoms triggered by a HFHS diet we conducted an oral glucose tolerance test (OGTT). No difference in fasting blood glucose levels between diet groups was observed (N = 30 (RD) / 29 (HFHS), median = 150 / 147 mg/dL). However, HFHS animals demonstrated impaired glucose intolerance upon application of an oral glucose dose; blood glucose levels 30 min, 60 min and 120 min after oral application were significantly increased compared to RD animals (**Fig 1 B**, N = 30 (RD) / 29 (HFHS), 30 minutes median = 265 / 313 mg/dL and 60 minutes median = 290 / 347 mg/dL, ordinary two-way ANOVA, followed by Sidak's multiple comparisons test, p = 0.0004, p = 0.0009, respectively). We compared the insulin

response after application of oral glucose load and found no difference between the diet regimens. The insulin resistance index (fasting glucose level (mmol/L) x fasting insulin level (mIU/L) showed no significant differences (**Fig 1 C,** N = 30 (RD) / 29 (HFHS), Mann-Whitney test, p = 0.6871) (Hayashi et al., 2013; Li et al., 2009). Five animals were euthanized pre-challenge in order to assess diet induced pathology. There was no difference in body fat-to-weight ratio (**Fig 1 D**, N = 5, median = 1.905 (RD) / 2.117 (HFHS) Fat:Bodyweight ratio (mg/g), Mann-Whitney test, p > 0.9999).

High-fat and high-sugar diet induces liver damage and systemic hyperlipidemia

We investigated the changes in lipid metabolism through a blood lipid biochemistry panel (**Sup Table 1**). Due to increased levels of fat in the samples collected from HFHS animals, HDL and LDL could not be assessed due to incompatibility with the instrument. Total cholesterol was significantly increased in the HFHS group (**Fig 1 E**, N = 10 (RD) / 7 (HFHS), median = 67.6 / 380 mg/dL, Mann-Whitney test, p = 0.0001). The median (146 U/L) alanine aminotransferase (ALT), an indication of hepatocellular injury without overt cholestasis, values in the HFHS animals were above the upper limit of previously established reference ranges (Washington and Van Hoosier, 2012). To understand which lipids were circulating in serum, we analyzed serum by liquid chromatography tandem mass spectrometry (LC-MS/MS). Aggregate signals across all lipid classes assayed in the HFHS animals compared to RD were increased, comprising phospholipids, cholesterol esters, sphingolipids, neutral lipids, lysophospholipids, and free fatty acids **(Fig 1 F,** N = 5(RD) / 4 (HFHS), Mann-Whitney test, p = 0.0159, p = 0.0635, p = 0.0159, p = 0.0317, p = 0.0653, p = 0.0317, respectively). Hence, we further assessed changes in the liver through gross and histologic pathology. Gross pathology of livers differed substantially. Livers from animals on the HFHS diet were diffusely pale, friable, and sections floated in formalin while RD hamster livers appeared grossly normal. Histologically, hepatocytes were expanded by micro

and macrovesicles in HFHS animals, while hepatocytes in RD animals appeared normal (**Fig 2 A - F**).

To further characterize the effect of the HFHS diet regimen on the liver, we evaluated global changes in the gene expression after 16 weeks. Principal components analysis of the complete gene expression profile revealed expected grouping with each diet regimen group containing their associated replicates (**Sup Fig 1 A**, N = 5 (RD), 4 HFHS). In total, 2,114 genes were significantly, differentially expressed ($p<0.05$ and >2fold) in the liver. To assess the enrichment of these differential genes, they were imported into Ingenuity Pathway Analysis (IPA) software. The results show that in the comparison of HFHS to RD animals 124 canonical pathways were significantly enriched and 200 downstream effects were predicted on biological processes and disease or toxicological function (p-value < 0.05, z-score <= -2 or >= 2): amongst which were cell recruitment, inflammation, activation, and immune-associated pathways **(Fig 2 G, Sup Table** 2 shows all significant predicted downstream effects**).** Interestingly, we also observed a pathway activation pattern reminiscent of NAFLD TNF-driven inflammation, (**Fig 2 H**).

Together, these data suggest that HFHS diet induced drastic changes in glucose uptake and lipid metabolism, characterized by systemic dyslipidemia and gross changes in liver pathology. This translated into increased inflammation and a gene expression profile in the liver reminiscent of fatty liver disease.

High-fat and high-sugar diet exacerbated disease severity after SARS-CoV-2 infection

We challenged hamsters (RD: N = 20, HFHS = 13 (Group size adjusted for the HFHS group due to the morbidity of the model pre-challenge)) with $8x10^4$ $TCID_{50}$ SARS-CoV-2 via the intranasal route. Animals were euthanized at 7 days-post inoculation (DPI) (RD: N = 10, HFHS = 4), at 14 DPI (RD: N = 5, HFHS = 4) or monitored until 21 DPI (RD: N = 5, HFHS = 5). We observed a trend of more severe morbidity in the HFHS group, in which two animals reached euthanasia criteria (>20% relative body weight loss) at 8 and 9 DPI, respectively (**Fig 3 A**). While the HFHS

142 animals demonstrated non-infection associated morbidity, the timing and symptoms associated
143 with these fatalities suggest that they were caused by the infection. In the RD group, a median
144 peak weight loss was observed at 6 DPI (~7% relative body weight), after which animals
145 recovered and returned to pre-challenge weights by 14 DPI. Weight in HFHS animals was
146 significantly decreased after 3 DPI and negative area under the curve (AUC) analysis between 1
147 -14 DPI revealed significant difference (**Fig 3 B,** N = 10 (RD) / 7 (HFHS), Mann-Whitney test, p =
148 0.0002). In the HFHS group median peak weight loss was reached at 8 DPI (~16% relative body
149 weight) and no animal recovered pre-challenge weights until the end of the study at 21 DPI.
150 To better understand the clinical impact of a HFHS diet on SARS-CoV-2 infection, the respiratory
151 function of the hamsters was evaluated. We performed forced oscillation tests on mechanically
152 ventilated hamsters pre-challenge, and on 7, 14, and 21 DPI. No significant differences in
153 pulmonary function were detected between the RD and HFHS groups at any time point.
154 Pulmonary function after SARS-CoV-2 infection has not been assessed in the Syrian hamster yet,
155 so we combined the groups to evaluate changes over the course of infection. Inspiratory capacity
156 was significantly decreased in 7 DPI as compared to pre-challenge **(Figure 3 C**, baseline: N = 5
157 (RD) / 3 (HFHS) and 7 DPI: N = 5 (RD) / 4 (HFHS), baseline median = 4.345 / 4.032 and 7 DPI
158 median = 3.195 / 3.464 mL, ordinary two-way ANOVA, followed by Tukey's multiple comparisons
159 test, p = 0.0107). Elastance of the respiratory system was significantly increased at 7 DPI
160 (baseline median = 2.68 / 3.032 and 7 DPI median = 4.138 / 3.852 cmH2O/mL, p = 0.0022), as
161 was tissue elastance (baseline median = 2.514 / 2.450 and 7 DPI median = 3.021 / 3217
162 cmH2O/mL, p = 0.0040). The resistance of the airway not associated with gas exchange
163 (Newtonian resistance) was not significantly different at any time point; however total resistance
164 was significantly increased in 7 DPI as compared to pre-challenge (baseline median = 0.151 /
165 0.167 and 7 DPI median = 0.181 / 0.205 cmH2O.s/mL, p = 0.034). Changes in peripheral
166 resistance were also detected by an increase in tissue damping at 7 DPI as compared to pre-
167 challenge animals, which reflects how oscillatory energy is dispersed or retained within

parenchymal tissue (baseline median = 0.564 / 0.623 and 7 DPI median = 0.695 / 0.720 cmH2O/mL, p = 0.0158). Recovery to pre-challenge was observed for all parameters by 14 DPI. Together, these changes in respiratory function led to an overall decrease in shape parameter k, which reflects the curvature of the pressure-volume curve, on 7 DPI (**Fig 3 D**, baseline median = 0.193 / 0.180 and 7 DPI median = 0.168 / 0.158 /cmH_20, ordinary two-way ANOVA, followed by Sidak's multiple comparisons test, p = 0.0001). While not significant, a slower trend of recovery to pre-challenge values for resistance and tissue damping was observed in the HFHS group. This could indicate that functional lung recovery in this group was slower.

High-fat and high-sugar diet is associated with exudate, vasculitis, inflammation of the epithelia and hemorrhage, fibrin and edema, and decreased viral clearance

Next, we assessed the pathology in the lungs at necropsy, 7 DPI. Grossly, lungs displayed lesions with multifocal dark red foci visible on the surface of the lobes (**Fig 4 A-J**). Across groups the 7 DPI lungs were more turgid, failed to collapse and had increased lung weights as compared to pre-challenge lungs (**Sup Fig 2 A**). Lung weight recovery appeared slower in HFHS animals. Histopathologically, only a subset of RD animals demonstrated increased lung damage (N = 5/10, > 50% lung tissue affected). At 7 DPI, foci were multifocal and adjacent to bronchi and blood vessels as well as peripherally along the sub pleural margin. Overall, no significant difference was seen between the cumulative pathological score between diet groups. However, three out of four animals demonstrated lesions in >50% of tissue (**Fig 4 K, Sup Fig 2 B**). In HFHS animals, foci were multifocal but less clearly delineated due to hemorrhage, edema, and fibrin. Interstitial pneumonia was characterized by thickened septa due to inflammatory cells, fibrin and edema and lined by hyperplastic type II pneumocytes. Alveoli were filled with inflammatory cells, edema and organizing fibrin. The two HFHS animals which were euthanized at day 8/9 due to severe disease and weight loss (>20%) both showed pneumonia, hemorrhage, edema, and inflammation (**Sup Fig 3**).

At 14 DPI, thickened septa, presumably from interstitial fibrosis with alveolar bronchiolization, were observed in lungs from RD animals (N = 2) (**Sup Fig 4 A-D**). In contrast, HFHS animals at 14 DPI had less septal thickening and more septal, alveolar, and perivascular inflammation (N = 2). At 21 DPI four out of five of the RD animals and three out of three of the HFHS animals had thickened alveolar septa with alveolar bronchiolization (**Sup Fig 4 E-H**).

Immunohistochemistry staining for SARS-CoV-2 antigen was increased at 7 DPI in lungs of HFHS animals compared to RD animals (median = 2.71 (RD) / 5.043 (HFHS), N = 10 / 4) (**Fig 4 E.J.L**). To confirm this finding, we compared genomic RNA, subgenomic (sg)RNA (surrogate for replicating virus) and infectious viral particles isolated from lungs at 7 DPI. Levels of gRNA and sgRNA in the lungs of HFHS animals at 7 DPI were significantly increased as compared to RD animals. Additionally, no infectious virus could be isolated from a subset of RD animals and overall, significantly more infectious virus could be isolated in HFHS animals (**Fig 4 M.N.O**; RD: N = 10, HFHS: N = 4, gRNA median = 6.935 / 8.513 copies/g lung (log_{10}), sgRNA median = 5.639 / 7.896 copies/g lung (log_{10}) and infectious virus median = 1.63 / 3.703 $TCID_{50}$/g (log_{10}), Mann-Whitney test, p = 0.0240, p = 0.0240 and p = 0.0120, respectively).

To better understand if the HFHS diet contributed to changes in viral replication kinetics in the upper respiratory tract, swabs from the oropharynx were analyzed for the presence of sgRNA. Respiratory shedding in both groups peaked at 2 DPI. Shedding in HFHS animals was constantly high up until 10 DPI, while shedding began decreasing in RD animals after 6 DPI. To compare the overall shedding burden, we performed an area under the curve (AUC) analysis for both groups depicting the cumulative shedding. HFHS animals presented significantly higher cumulative shedding (**Fig 4 P.Q**, N = 5 (RD) / 3 (HFHS), median 41.48 / 44.44 AUC (log_{10}), Mann-Whitney test, p = 0.0357).

Immune infiltration in the lung during the acute-phase of infection and humoral immunity are not significantly affected by high-fat high-sugar diet

Using immunohistochemistry, we investigated the infiltration of macrophages (IBA 1 staining), T-cells (CD3 staining), and B-cells (Pax 5 staining) over the course of infection (**Fig 5**). Macrophages were detected throughout all sections but were increased in 7 and 14 DPI samples in pneumonic areas irrespective of diet regimen. In addition, T lymphocytes were increased in 7 and 14 DPI samples in pneumonic areas. No increase in B cells was observed. To quantify the influx of macrophages and T cells we used morphometric analysis (**Sup Fig 5**). No significant difference was seen between the RD and HFHS groups. Both macrophages and T cells increased in numbers at 7 DPI as compared to pre-challenge conditions for both groups. **(Fig 6 A.B**, pre-challenge: N = (RD) / 2 (HFHS) and 7 DPI: N = 10 (RD) / 4 (HFHS), median macrophages = (3.075 / 3.530 (pre-challenge)) / (13.630 / 10.480 (7 DPI)) % reactivity and median T cells = (4.515 / 4.125 (pre-challenge)) / (11.340 / 11.255 (7 DPI)) % reactivity, ordinary two-way ANOVA, followed by Sidak's multiple comparisons test, p = 0.1007 / 0.3564 and p = 0.0001 / 0.0001, respectively).

The humoral response to SARS-CoV-2 was not significantly impacted by diet regimen. Animals seroconverted at 7 DPI, as measured by anti-spike IgG ELISA (**Fig 6 C,** 7 DPI: N = 10 (RD) / 4 (HFHS), 14 DPI: N = 5 (RD) / 4 (HFHS), 21 DPI: N = 5 (RD) / 3 (HFHS), ordinary two-way ANOVA, followed by Tukey's multiple comparisons test, p = 0.8573, p = 0.8203 and p = 0.5468, respectively). Neutralization of virus by sera collected at 14 and 21 DPI was compared to assess potential differences in affinity maturation and no significant difference was found (**Fig 6 D,** 14 DPI: N = 5 (RD) / 4 (HFHS), 21 DPI: N = 5 (RD) / 3 (HFHS), 14 DPI median = 120 / 80 and 21 DPI median = 120/120 reciprocal titer, ordinary two-way ANOVA, followed by Tukey's multiple comparisons test, p = 0.5535 and p = 0.4688, respectively).

Prolonged SARS-CoV-2 shedding, systemic immune and metabolomic dysregulation after high-fat high-sugar diet

The cytokine kinetics were analyzed in serum throughout the course of infection by ELISA. Serum samples were collected pre-challenge (0 DPI), on 7 DPI, 14 DPI and 21 DPI (**Fig 6 E**). Pro-inflammatory tumor necrosis factor (TNF)-α, interleukin (IL)-6, antiviral interferon (IFN)-γ, and (IL)-10 did not significantly differ between diet regimens pre-challenge. After infection, RD animals mounted a significant IFN-γ response which lasted into recovery (14 and 21 DPI), while no response was seen in HFHS animals (RD: N = 5/10, HFHS: N = 4, pre-challenge median = 629 / 618, 7 DPI median = 737.85 / 550.6, 14 DPI median = 702.3 / 623.55, 21 DPI median = 1042.3 / 609.8 pg/mL, ordinary two-way ANOVA, followed by Sidak's multiple comparisons test, pre-challenge: $p = 0.58157$, 7 DPI: $p = 0.0090$, 14 DPI: $p = 0.7373$, 21 DPI $p < 0.0001$). In contrast, serum IL-6 trended higher in HFHS animals compared to RD animals at 7 DPI (median = 2795.5 (RD) / 2859.2 (HFHS) pg/mL). This trend toward higher IL-6 continued at 14 and 21 DPI. IL-10 levels trended higher in HFHS animals during the acute phase and remained elevated at 14 DPI (RD: N = 5/10, HFHS: N = 4, pre-challenge median = 1894.6 / 2131.5, 7 DPI median = 2071.75 / 2773.95, 14 DPI median = 1768.5 / 2354.35, 21 DPI median = 1733.7 / 2407.6 pg/mL ordinary two-way ANOVA, followed by Sidak's multiple comparisons test, pre-challenge: $p = 0.9933$, 7 DPI: $p = 0.0548$, 14 DPI: $p = 0.1408$, 21 DPI $p = 1259$). TNF-α serum levels demonstrated an ambivalent pattern.

To examine compositional changes in the circulating lipidome over the course of infection, the lipidome was analyzed between 0 DPI and 7 DPI of infection. This analysis revealed distinct lipid dynamics in response to SARS-CoV-2 infection (**Fig 6 F).** RD animals displayed a serum lipid shift in response to infection consisting primarily of decreased levels of phospholipids with mixed representation of lipid classes and a distribution of long chain and polyunsaturated fatty acids (PUFA). HFHS serum displayed a more drastic pattern of lipid depletion and enrichment.

Specifically, HFHS serum reflected a sharp enrichment of free polyunsaturated fatty acids (PUFA) and a combination of enrichment and depletion of PUFA containing phospholipids. This response peaked at 7 DPI and began to return to homeostasis by 14 DPI, though certain lipid patterns were carried out until 21 DPI.

Discussion

The development of animal models that faithfully recapitulate certain aspects of human disease remains a top priority in SARS-CoV-2 research. Healthy Syrian hamsters develop mild to moderate disease similar to the majority of human cases; however, they do not exhibit the more severe respiratory disease seen in humans with comorbidities such as obesity, diabetes, or other chronic illness (Araújo et al., 2019; Hussain et al., 2020; Korakas et al., 2020). Thus, we developed an experimental infection model of hamsters exclusively fed a high-fat high-sugar diet to model the impact of Western Diet on COVID-19 severity. In the Syrian hamster, this diet caused diet-induced morbidity, led to increased weight gain during adolescence, and ultimately led to in increased glucose tolerance, systemic hyperlipidemia, increased total cholesterol and a liver pathology reminiscent of a NAFLD-like phenotype. The lack of net weight gain in this model may present a means of decoupling liver associated pathologies such as NAFLD from obesity-associated disease more broadly. In humans NAFLD is predominantly a consequence of obesity and frequently associated also with other comorbidities as well (Sanyal, 2019). In the context of COVID-19, NAFLD is associated with increased hospitalization and disease severity (Bramante et al., 2020).

The morbidity observed in the absence of infection in the HFHS group should be considered in future studies utilizing this model. In particular, this feature of the model may make survival-based studies difficult. Human clinical studies of COVID-19 are plagued by this same difficulty in quantifying the contribution of infection and the associated comorbidities to the eventual cause of death. If appropriately controlled for in this model the relative contribution to death from the

295 infection and the comorbidities can be quantified. We observed that male hamsters on a HFHS
296 diet demonstrated delayed lower and upper respiratory tract clearance after infection with SARS-
297 CoV-2, which was accompanied by more severe disease presentation. Our data is in agreement
298 with findings in mice, which have reported enhanced morbidity in aged and diabetic obese mice
299 in a mouse-adapted SARS-CoV-2 model (Rathnasinghe et al., 2021). Conversely, we also
300 observed increased weight loss, pathology, delayed lung recovery and influx of immune cells into
301 the lung in a subset of hamsters fed a regular diet as compared to what has been shown in
302 younger animals (Chan et al., 2020; Rosenke et al., 2020). This is likely due to the increased age
303 of the animals used in this study (Osterrieder et al., 2020). Previously, lung function analysis after
304 SARS-CoV-2 infection in a rodent model has only been demonstrated in ACE2 mice (Winkler et
305 al., 2020). While not significantly different between the diet groups, we performed functional lung
306 analysis for the first time in the Syrian hamster after SARS-CoV-2 infection and demonstrated
307 that this model also recapitulates increased total airway resistance and decreased inspiratory
308 capacity. This suggests that the Syrian hamster, besides recapitulating lung pathology, may also
309 be a useful model for mechanistic studies of the respiratory parameters affected by COVID-19.
310 Importantly, the HFHS Syrian hamster model presented here recapitulated two key mediators of
311 severe human COVID-19. One unique feature of the cytokine profile in human disease is the
312 elevation of IL-6 and IL-10, which have been indicated as causes of increased pathology (Chen
313 et al., 2020; Dhar et al., 2020; Lu et al., 2021; Wang et al., 2020). In line with this, in HFHS animals
314 we observed trending increases in serum IL-10 and IL-6 levels after infection. Secondly, in
315 response to infection, HFHS animals showed a more severe response in their serum lipids at 7
316 DPI compared to RD animals. The lipids that dominated this response were free-PUFAs and
317 PUFA-containing phosphatidylethanolamine (PE). In addition, we saw mixed increase and
318 decrease of PUFA-containing plasmalogens and triacylglycerols. The metabolic comorbidities
319 associated with severe COVID-19 were previously shown to correlate with specific mobilization
320 of serum lipids in a human cohort (Schwarz et al., 2020). Specifically, disease severity, defined

by ICU admittance, was shown to be associated with increased free PUFAs and PUFA-containing phosphatidylethanolamine, as well as a decrease of PUFA-containing phosphatidylcholine and plasmalogen, compared to non-ICU hospitalized patients. These imbalances were reflected in the circulating milieu of immune-active, PUFA-derived lipid mediators in these patients. The lipid pattern findings in the Syrian hamster model suggest that these serum lipid changes are dependent on preexisting serum hyperlipidemia and stimulated by infection with SARS-CoV-2. Despite the lack of obesity in these animals, the matching of clinical SARS-CoV-2-associated lipid patterns and cytokine profile in this model supports its utility in examining lipid and inflammation dynamics associated immune dysregulation during infection.

Of note, this did not seem to adversely affect the humoral immune response while viral titers in oropharyngeal swabs and lung tissues suggested delayed clearance in the HFHS group. This may indicate that other immune pathways were disproportionately affected, but further investigations would be necessary to draw concrete conclusions.

Taking the limitations of the model into account, our data further suggests the possible suitability of the Syrian hamster model to assess immunomodulatory therapies. While dietary advice for those suffering from metabolic diseases is proposed to reduce burden of severe COVID-19 (Demasi, 2021), it remains doubtful if any change in diet can impact disease outcome favorably after infection has occurred. Targeted immunomodulatory therapies, such as anti-IL-6 therapies, may be more efficient (Zhong et al., 2020). The Syrian hamster model may also be applied to further studies of selected aspects of NAFLD, which the model recapitulates. This model seems to present with an absences or limited amount of liver fibrosis; further work is needed to demonstrate how faithfully it assesses the direct effect of liver fibrosis on acute disease. However, it may be useful to assess long term post-COVID-19 NAFLD, to document further deterioration of liver damage (Portincasa et al., 2020) and the relation to infection sequelae.

Acknowledgements

The authors would like to thank Kwe Claude Yinda and Robert Fisher for technical support, the Rocky Mountain Veterinary branch, including Marissa Woods, Nicki Arndt, Amanda Weidow, Linda Couey and Brian Mosbrucker for assistance with high containment husbandry, Tina Thomas, and Rebecca Rosenke for assistance with histology and Danielle Hopkins for flexiVent support and Kathryn Willebrand and Taylor Saturday for assistance with manuscript editing. This research was supported by the Intramural Research Program of the National Institute of Allergy and Infectious Diseases (NIAID), National Institutes of Health (NIH).

Author Contributions

Conceptualization, J.R.P.;
Methodology, J.R.P., D.R.A., and B.S.;
Investigation, J.R.P., D.R.A.,B.S, J.E.S., V.A.A., M.G.H., J.N.P., D.S, K.A.S., I.L., B.J.S., C.S.;
Writing – Original Draft, J.R.P., D.R.A., B.S., C.S.;
Writing – Review & Editing, J.R.P., D.R.A. and V.J.M.;
Funding Acquisition, VJ..M.;
Resources, V.A.A., B.S., B.J.S. and C.M.B.;
Supervision, V.J.M.

Declaration of Interest

The authors declare no competing financial interests.

Methods

Ethics statement

Approval of animal experiments was obtained from the Institutional Animal Care and Use Committee of the Rocky Mountain Laboratories. Performance of experiments was done following the guidelines and basic principles in the United States Public Health Service Policy on Humane Care and Use of Laboratory Animals and the Guide for the Care and Use of Laboratory Animals. Work with infectious SARS-CoV-2 strains under BSL3 conditions was approved by the Institutional Biosafety Committee (IBC). Inactivation and removal of samples from high

containment was performed per IBC-approved standard operating procedures (Haddock et al., 2021).

Virus and cells

SARS-CoV-2 strain nCoV-WA1-2020 (MN985325.1) was provided by CDC, Atlanta, USA. Virus propagation was performed in VeroE6 cells in DMEM supplemented with 2% foetal bovine serum (FBS), 2 mM L-glutamine, 100 U/mL penicillin and 100 µg/mL streptomycin. VeroE6 cells were maintained in DMEM supplemented with 10% FBS, 2 mM L-glutamine, 100 U/mL penicillin and 100 µg/mL streptomycin D10. Virus stock was 100% identical to the initial sequence (MN985325.1) and no contaminants were detected.

High-fat high-sugar diet

Four to six-week-old male Syrian Golden hamsters (ENVIGO) were randomly assigned to either regular rodent chow (Teklad Global 16% Protein Rodent Diet, Envigo) or a HFHS diet for 16 weeks (Purina Chow #5001 with 11.5% Corn Oil, 11.5% Coconut Oil, 0.5% Cholesterol, 0.25% Deoxycholic Acid, and 10% Fructose: Dyets Inc., Dyet#615088). Pre-challenge oral glucose tests were performed on all animals. Five animals from each diet group were euthanized after the 16 wks for collection of pre-challenge tissue samples and weights. For each diet group, 5 animals were randomly designated for flexiVent calibration and excluded from further analysis. Three animals in the HFHS regimen were euthanized throughout the 16-week diet regimen due to secondary morbidities and were not included in analyses. Pre-challenge, an additional 5 animals in the RD group and additional 8 animals in the HFHS group were excluded from the study due to experimental reasons, and one animal in the HFHS group due to secondary morbidities.

Assessment of glucose tolerance

An oral glucose tolerance test (OGTT) was performed after 16 weeks of diet manipulation (Dalbøge et al., 2015). Hamsters were fasted for 16 h overnight preceding the OGTT. An oral glucose load (2 g/kg glucose) was administered. Blood samples were collected from the retroorbital sinus using capillary tube at 0-, 30-, 60-, and 120-min post glucose administration. Blood glucose was measured using the AlphaTRAK blood glucose monitoring system (Zoetis), calibrated for cats. Serum was separated and used for measurement of insulin. Insulin was measured using the rat/mouse insulin ELISA kit from Millipore (EZRMI-13K), according to the manufacturer's instructions (Wang et al., 2001).

Lipidomics

Blood lipids were assessed for a subset of animals (N= 8-10) after 16 weeks of diet. 200 µL blood was collected and were measured using the Piccolo® Lipid Panel Plus for humans (Abraxis) according to the manufacturer's instruction.

Next-generation sequencing of liver mRNA

Frozen tissues were pulverized in 1 mL of Trizol (Thermofisher Scientific), 200 µL of 1-Bromo-3-chloropropane (MilliporeSigma) was added, samples mixed, and centrifuged at 16,000 x *g* for 15 min at 4 °C. RNA containing aqueous phase of 600 µL was collected from each sample and passed through Qiashredder column (Qiagen) at 21,000 x g for 2 min to homogenize any remaining genomic DNA in the aqueous phase. Aqueous phase was combined with 600 µL of RLT lysis buffer (Qiagen, Valencia, CA) with 1% beta mercaptoethanol (MilliporeSigma) and RNA was extracted using Qiagen AllPrep DNA/RNA 96-well system. An additional on-column DNase-1 treatment was performed during RNA extraction. RNA was quantitated by spectrophotometry and yield ranged from 0.4 to 17.8 µg. One hundred nanograms of RNA was used as input for rRNA depletion and NGS library preparation following the Illumina Stranded Total RNA Prep Ligation with Ribo-Zero Plus workflow (Illumina). The NGS libraries were prepared, amplified for

13 cycles, AMPureXP bead (Beckman Coulter) purified using 0.95X beads, assessed on a BioAnalyzer DNA1000 chip (Agilent Technologies) and quantified using the Kapa Quantification Kit for Illumina Sequencing (Roche). Amplified libraries were pooled at equal molar amounts and sequenced on a NextSeq (Illumina) using two High Output 150 cycle chemistry kits. Raw fastq reads were trimmed of Illumina adapter sequences using cutadapt version 1.12 and then trimmed and filtered for quality using the FASTX-Toolkit (Hannon Lab). Remaining reads were aligned to the *Mesocricetus auratus* genome assembly version 1.0 using Hisat2 (Kim et al., 2015). Reads mapping to genes were counted using htseq-count (Anders et al., 2015). Differential expression analysis was performed using the Bioconductor package DESeq2 (Love et al., 2014). Pathway analysis was performed using Ingenuity Pathway Analysis (QIAGEN) and gene clustering was performed using Partek Genomics Suite (Partek Inc.). Samples with too low quality were removed from the analysis (Sup Table 1).

Next-generation sequencing of virus

For sequencing from viral stocks, sequencing libraries were prepared using Stranded Total RNA Prep Ligation with Ribo-Zero Plus kit per manufacturer's protocol (Illumina) and sequenced on an Illumina MiSeq at 2 x 150 base pair reads. For sequencing from swab and lung tissue, total RNA was depleted of ribosomal RNA using the Ribo-Zero Gold rRNA Removal kit (Illumina). Sequencing libraries were constructed using the KAPA RNA HyperPrep kit following manufacturer's protocol (Roche Sequencing Solutions). To enrich for SARS-CoV-2 sequence, libraries were hybridized to myBaits Expert Virus biotinylated oligonucleotide baits following the manufacturer's manual, version 4.01 (Arbor Biosciences). Enriched libraries were sequenced on the Illumina MiSeq instrument as paired-end 2 X 150 base pair reads. Raw fastq reads were trimmed of Illumina adapter sequences using cutadapt version 1.1227 and then trimmed and filtered for quality using the FASTX-Toolkit (Hannon Lab, CSHL). Remaining reads were mapped to the SARS-CoV-2 2019-nCoV/USA-WA1/2020 genome (MN985325.1) using Bowtie2 version

454 2.2.928 with parameters --local --no-mixed -X 1500. PCR duplicates were removed using picard
455 MarkDuplicates (Broad Institute) and variants were called using GATK HaplotypeCaller version
456 4.1.2.029 with parameter -ploidy 2. Variants were filtered for QUAL > 500 and DP > 20 using
457 bcftools.
458
459 *Inoculation experiments*
460 After 16 weeks, animals were then inoculated intranasally (I.N.) under isoflurane anaesthesia. I.N.
461 inoculation was performed with 40 µL sterile Dulbecco's Modified Eagle Medium (DMEM)
462 containing $8x10^4$ $TCID_{50}$ SARS-CoV-2. A subset of animals (N= 4-10) were euthanized, and
463 serum and tissues were collected at pre-challenge (0 DPI), 4, 7, 14, and 21 DPI. Hamsters were
464 weighted daily, and oropharyngeal swabs (21 DPI animals only) were taken daily until day 7 and
465 then thrice a week. Swabs were collected in 1 mL DMEM with 200 U/mL penicillin and 200 µg/mL
466 streptomycin. Hamsters were observed daily for clinical signs of disease.
467
468 *Lung function analyses*
469 Lung function assessment was performed on pre-challenge, 7, 14, and 21 DPI. Hamsters were
470 anesthetized with a combination of inhalant isoflurane and ketamine/xylazine intraperitoneally.
471 After animals reached a surgical plane of anaesthesia a terminal tracheostomy was performed as
472 previously described (McGovern TK JOVE 2013). Briefly, a cannula was introduced into the
473 trachea, secured with suture, and the animal underwent the forced oscillation technique (FOT)
474 using a flexiVent (SCIREZ, Inc.). Animals were kept at a consistent surgical plane of anesthesia
475 to the point of not resisting the FOT procedure. Animals were immediately euthanized while
476 deeply anesthetized after FOT was completed; the surgical procedure was terminal.
477
478 *Histopathology and immunohistochemistry*

Necropsies and tissue sampling were performed according to IBC-approved protocols. Tissues were fixed for a minimum of 7 days in 10% neutral buffered formalin with 2 changes. Tissues were placed in cassettes and processed with a Sakura VIP-6 Tissue Tek, on a 12-hour automated schedule, using a graded series of ethanol, xylene, and ParaPlast Extra. Prior to staining, embedded tissues were sectioned at 5 µm and dried overnight at 42°C. Using GenScript U864YFA140-4/CB2093 NP-1 (1:1000) specific anti-CoV immunoreactivity, CD3 (Predilute) (Roche Tissue Diagnostics #790-4341), and PAX5 (1:500) (Novus Biologicals #NBP2-38790) were detected using the Vector Laboratories ImPress VR anti-rabbit IgG polymer (# MP-6401) as the secondary antibody. Iba-1 (1:500) (abcam #ab5076) was detected using Roche Tissue Diagnostics OmniMap anti-goat multimer (#760-4647) as the secondary antibody. The tissues were stained using the Discovery Ultra automated stainer (Ventana Medical Systems) with a ChromoMap DAB kit Roche Tissue Diagnostics (#760-159).

Morphometric analysis.

IHC stained tissue slides were scanned with an Aperio ScanScope XT (Aperio Technologies, Inc.) and analyzed using the ImageScope Positive Pixel Count algorithm (version 9.1). The default parameters of the Positive Pixel Count (hue of 0.1 and width of 0.5) detected antigen adequately.

Viral RNA detection

Swabs from hamsters were collected as described above. Cage and bedding material was sampled with prewetted swabs in 1 mL of DMEM supplemented with 200 U/mL penicillin and 200 µg/mL streptomycin. Then, 140 µL was utilized for RNA extraction using the QIAamp Viral RNA Kit (Qiagen) using QIAcube HT automated system (Qiagen) according to the manufacturer's instructions with an elution volume of 150 µL. Sub-genomic (sg) viral RNA and genomic (g) was detected by qRT-PCR (Corman et al., 2020a; Corman et al., 2020b). Five µL RNA was tested with TaqMan™ Fast Virus One-Step Master Mix (Applied Biosystems) using QuantStudio 6 Flex

Real-Time PCR System (Applied Biosystems) according to instructions of the manufacturer. Ten-fold dilutions of SARS-CoV-2 standards with known copy numbers were used to construct a standard curve and calculate copy numbers/mL.

Viral titration

Viable virus in tissue samples was determined as previously described (van Doremalen et al., 2017). In brief, lung tissue samples were weighted, then homogenized in 1 mL of DMEM2. VeroE6 cells were inoculated with ten-fold serial dilutions of tissue homogenate, spun at 1000 rpm for 1 h at 37 °C, the first dilutions washed with PBS and with DMEM2. Cells were incubated with tissue homogenate for 6 days at 37 °C, 5% CO_2, then scored for cytopathic effect. $TCID_{50}$ was calculated by the method of Spearman-Karber and adjusted for tissue weight.

Serology

Serum samples were inactivated with γ-irradiation (2 mRad) and analyzed as previously described (Yinda et al., 2020). In brief, maxisorp plates (Nunc) were coated with 50 ng spike protein (generated in-house) per well and incubated overnight at 4 °C. After blocking with casein in phosphate buffered saline (PBS) (ThermoFisher) for 1 h at room temperature (RT), serially diluted 2-fold serum samples (duplicate, in blocking buffer) were incubated for 1 h at RT. Spike-specific antibodies were detected with goat anti-hamster IgG Fc (horseradish peroxidase (HRP)-conjugated, Abcam) for 1 h at RT and visualized with KPL TMB 2-component peroxidase substrate kit (SeraCare, 5120-0047). The reaction was stopped with KPL stop solution (Seracare) and read at 450 nm. Plates were washed 3 to 5 x with PBS-T (0.1 % Tween) for each wash. The threshold for positivity was calculated as the average plus 3 x the standard deviation of negative control hamster sera.

Cytokine analysis

Cytokine concentrations were determined using a commercial hamster ELISA kit for TNF-α, INF-γ, IL-6, IL-4, and IL-10 available at antibodies.com, according to the manufacturer's instructions (antibodies.com; A74292, A74590, A74291, A74027, A75096). Samples were pre-diluted 1:10.

Serum lipid analysis

For abundance analysis of serum lipids signals were filtered using a 50 % miss value cut off and applying a raw intensity cutoff appropriate to the noise level of each class of lipids. Signals were then normalized to internal deuterated SPLASH® LIPIDOMIX® Mass Spec Standard (Avanti Polar Lipids). For compositional analysis of the serum, bulk lipid datasets were further filtered using a 30 % QC coefficient of variance cut off prior to normalizing by the total signal sum. All univariate and multivariate analysis was performed using GraphPad Prism or MarkerView (AB Sciex). All parallel univariate analysis was subjected to a Benjamini-Hochberg correction using a false discovery rate of 15 %.

Statistical analysis

All graphs were designed in GraphPad Prism software (version 8.0.1; GraphPad Software). Significance test were performed as indicated where appropriate. Statistical significance levels were determined as follows: ns = $p > 0.05$; * = $p \leq 0.05$; ** = $p \leq 0.01$; *** = $p \leq 0.001$; **** = $p \leq 0.0001$.

References

Anders, S., Pyl, P.T., and Huber, W. (2015). HTSeq--a Python framework to work with high-throughput sequencing data. Bioinformatics *31*, 166-169.

557 Araújo, J., Cai, J., and Stevens, J. (2019). Prevalence of Optimal Metabolic Health in American Adults:
558 National Health and Nutrition Examination Survey 2009-2016. Metab Syndr Relat Disord *17*, 46-52.
559 Bramante, C., Tignanelli, C.J., Dutta, N., Jones, E., Tamariz, L., Clark, J.M., Usher, M., Metlon-Meaux,
560 G., and Ikramuddin, S. (2020). Non-alcoholic fatty liver disease (NAFLD) and risk of hospitalization for
561 Covid-19. medRxiv.
562 Butler, M.J., and Barrientos, R.M. (2020). The impact of nutrition on COVID-19 susceptibility and long-
563 term consequences. Brain Behav Immun *87*, 53-54.
564 Cefalu, W.T., and Rodgers, G.P. (2021). COVID-19 and metabolic diseases: a heightened awareness of
565 health inequities and a renewed focus for research priorities. Cell Metabolism *33*, 473-478.
566 Chan, J.F.-W., Zhang, A.J., Yuan, S., Poon, V.K.-M., Chan, C.C.-S., Lee, A.C.-Y., Chan, W.-M., Fan, Z.,
567 Tsoi, H.-W., Wen, L.*, et al.* (2020). Simulation of the Clinical and Pathological Manifestations of
568 Coronavirus Disease 2019 (COVID-19) in a Golden Syrian Hamster Model: Implications for Disease
569 Pathogenesis and Transmissibility. Clinical Infectious Diseases.
570 Chen, G., Wu, D., Guo, W., Cao, Y., Huang, D., Wang, H., Wang, T., Zhang, X., Chen, H., Yu, H.*, et al.*
571 (2020). Clinical and immunological features of severe and moderate coronavirus disease 2019. J Clin
572 Invest *130*, 2620-2629.
573 Cordain, L., Eaton, S.B., Sebastian, A., Mann, N., Lindeberg, S., Watkins, B.A., O'Keefe, J.H., and
574 Brand-Miller, J. (2005). Origins and evolution of the Western diet: health implications for the 21st
575 century. Am J Clin Nutr *81*, 341-354.
576 Corman, V.M., Landt, O., Kaiser, M., Molenkamp, R., Meijer, A., Chu, D.K., Bleicker, T., Brünink, S.,
577 Schneider, J., Schmidt, M.L.*, et al.* (2020a). Detection of 2019 novel coronavirus (2019-nCoV) by real-
578 time RT-PCR. Euro surveillance : bulletin Europeen sur les maladies transmissibles = European
579 communicable disease bulletin *25*, 2000045.
580 Corman, V.M., Landt, O., Kaiser, M., Molenkamp, R., Meijer, A., Chu, D.K., Bleicker, T., Brunink, S.,
581 Schneider, J., Schmidt, M.L.*, et al.* (2020b). Detection of 2019 novel coronavirus (2019-nCoV) by real-
582 time RT-PCR. Euro Surveill *25*.
583 Dalbøge, L.S., Pedersen, P.J., Hansen, G., Fabricius, K., Hansen, H.B., Jelsing, J., and Vrang, N. (2015).
584 A Hamster Model of Diet-Induced Obesity for Preclinical Evaluation of Anti-Obesity, Anti-Diabetic and
585 Lipid Modulating Agents. PloS one *10*, e0135634-e0135634.
586 Demasi, M. (2021). COVID-19 and metabolic syndrome: could diet be the key? BMJ Evidence-Based
587 Medicine *26*, 1-2.
588 Dhar, S.K., K, V., Damodar, S., Gujar, S., and Das, M. (2020). IL-6 and IL-10 as predictors of disease
589 severity in COVID 19 patients: Results from Meta-analysis and Regression. medRxiv,
590 2020.2008.2015.20175844.
591 Green, W.D., and Beck, M.A. (2017a). Obesity altered T cell metabolism and the response to infection.
592 Curr Opin Immunol *46*, 1-7.
593 Green, W.D., and Beck, M.A. (2017b). Obesity Impairs the Adaptive Immune Response to Influenza
594 Virus. Ann Am Thorac Soc *14*, S406-s409.
595 Haddock, E., Feldmann, F., Shupert, W.L., and Feldmann, H. (2021). Inactivation of SARS-CoV-2
596 Laboratory Specimens. Am J Trop Med Hyg *104*, 2195-2198.
597 Hayashi, T., Boyko, E.J., Sato, K.K., McNeely, M.J., Leonetti, D.L., Kahn, S.E., and Fujimoto, W.Y.
598 (2013). Patterns of insulin concentration during the OGTT predict the risk of type 2 diabetes in Japanese
599 Americans. Diabetes Care *36*, 1229-1235.
600 Hussain, A., Mahawar, K., Xia, Z., Yang, W., and El-Hasani, S. (2020). Obesity and mortality of
601 COVID-19. Meta-analysis. Obes Res Clin Pract *14*, 295-300.
602 Kasim-Karakas, S.E., Vriend, H., Almario, R., Chow, L.C., and Goodman, M.N. (1996). Effects of
603 dietary carbohydrates on glucose and lipid metabolism in golden Syrian hamsters. J Lab Clin Med *128*,
604 208-213.
605 Kim, D., Langmead, B., and Salzberg, S.L. (2015). HISAT: a fast spliced aligner with low memory
606 requirements. Nature Methods *12*, 357-360.

607 Korakas, E., Ikonomidis, I., Kousathana, F., Balampanis, K., Kountouri, A., Raptis, A., Palaiodimou, L.,
608 Kokkinos, A., and Lambadiari, V. (2020). Obesity and COVID-19: immune and metabolic derangement
609 as a possible link to adverse clinical outcomes. Am J Physiol Endocrinol Metab *319*, E105-e109.
610 Li, G., Liu, X., Zhu, H., Huang, L., Liu, Y., Ma, C., and Qin, C. (2009). Insulin resistance in insulin-
611 resistant and diabetic hamsters (Mesocricetus auratus) is associated with abnormal hepatic expression of
612 genes involved in lipid and glucose metabolism. Comp Med *59*, 449-458.
613 Love, M.I., Huber, W., and Anders, S. (2014). Moderated estimation of fold change and dispersion for
614 RNA-seq data with DESeq2. Genome Biology *15*, 550.
615 Lu, L., Zhang, H., Dauphars, D.J., and He, Y.-W. (2021). A Potential Role of Interleukin 10 in COVID-
616 19 Pathogenesis. Trends in Immunology *42*, 3-5.
617 Nie, S., Han, S., Ouyang, H., and Zhang, Z. (2020). Coronavirus Disease 2019-related dyspnea cases
618 difficult to interpret using chest computed tomography. Respir Med *167*, 105951-105951.
619 Osterrieder, N., Bertzbach, L.D., Dietert, K., Abdelgawad, A., Vladimirova, D., Kunec, D., Hoffmann,
620 D., Beer, M., Gruber, A.D., and Trimpert, J. (2020). Age-Dependent Progression of SARS-CoV-2
621 Infection in Syrian Hamsters. Viruses *12*.
622 Parry, A.H., Wani, A.H., Yaseen, M., Dar, K.A., Choh, N.A., Khan, N.A., Shah, N.N., and Jehangir, M.
623 (2020). Spectrum of chest computed tomographic (CT) findings in coronavirus disease-19 (COVID-19)
624 patients in India. Eur J Radiol *129*, 109147-109147.
625 Petrakis, D., Margină, D., Tsarouhas, K., Tekos, F., Stan, M., Nikitovic, D., Kouretas, D., Spandidos,
626 D.A., and Tsatsakis, A. (2020). Obesity - a risk factor for increased COVID-19 prevalence, severity and
627 lethality (Review). Mol Med Rep *22*, 9-19.
628 Portincasa, P., Krawczyk, M., Smyk, W., Lammert, F., and Di Ciaula, A. (2020). COVID-19 and non-
629 alcoholic fatty liver disease: Two intersecting pandemics. Eur J Clin Invest *50*, e13338.
630 Rathnasinghe, R., Jangra, S., Cupic, A., Martinez-Romero, C., Mulder, L.C.F., Kehrer, T., Yildiz, S.,
631 Choi, A., Mena, I., De Vrieze, J.*, et al.* (2021). The N501Y mutation in SARS-CoV-2 spike leads to
632 morbidity in obese and aged mice and is neutralized by convalescent and post-vaccination human sera.
633 medRxiv, 2021.2001.2019.21249592.
634 Rogero, M.M., and Calder, P.C. (2018). Obesity, Inflammation, Toll-Like Receptor 4 and Fatty Acids.
635 Nutrients *10*.
636 Rosenke, K., Meade-White, K., Letko, M., Clancy, C., Hansen, F., Liu, Y., Okumura, A., Tang-Huau,
637 T.L., Li, R., Saturday, G.*, et al.* (2020). Defining the Syrian hamster as a highly susceptible preclinical
638 model for SARS-CoV-2 infection. Emerg Microbes Infect, 1-36.
639 Saklayen, M.G. (2018). The Global Epidemic of the Metabolic Syndrome. Curr Hypertens Rep *20*, 12.
640 Sanyal, A.J. (2019). Past, present and future perspectives in nonalcoholic fatty liver disease. Nature
641 Reviews Gastroenterology & Hepatology *16*, 377-386.
642 Schwarz, B., Sharma, L., Roberts, L., Peng, X., Bermejo, S., Leighton, I., Casanovas-Massana, A.,
643 Minasyan, M., Farhadian, S., Ko, A.I.*, et al.* (2020). Cutting Edge: Severe SARS-CoV-2 Infection in
644 Humans Is Defined by a Shift in the Serum Lipidome, Resulting in Dysregulation of Eicosanoid Immune
645 Mediators. The Journal of Immunology, ji2001025.
646 Sia, S.F., Yan, L.M., Chin, A.W.H., Fung, K., Choy, K.T., Wong, A.Y.L., Kaewpreedee, P., Perera, R.,
647 Poon, L.L.M., Nicholls, J.M.*, et al.* (2020). Pathogenesis and transmission of SARS-CoV-2 in golden
648 hamsters. Nature.
649 Swinburn, B.A., Sacks, G., Hall, K.D., McPherson, K., Finegood, D.T., Moodie, M.L., and Gortmaker,
650 S.L. (2011). The global obesity pandemic: shaped by global drivers and local environments. The Lancet
651 *378*, 804-814.
652 van Doremalen, N., Falzarano, D., Ying, T., de Wit, E., Bushmaker, T., Feldmann, F., Okumura, A.,
653 Wang, Y., Scott, D.P., Hanley, P.W.*, et al.* (2017). Efficacy of antibody-based therapies against Middle
654 East respiratory syndrome coronavirus (MERS-CoV) in common marmosets. Antiviral Res *143*, 30-37.
655 Wang, J., Jiang, M., Chen, X., and Montaner, L.J. (2020). Cytokine storm and leukocyte changes in mild
656 versus severe SARS-CoV-2 infection: Review of 3939 COVID-19 patients in China and emerging
657 pathogenesis and therapy concepts. J Leukoc Biol.

Wang, P.-R., Guo, Q., Ippolito, M., Wu, M., Milot, D., Ventre, J., Doebber, T., Wright, S.D., and Chao, Y.-S. (2001). High fat fed hamster, a unique animal model for treatment of diabetic dyslipidemia with peroxisome proliferator activated receptor alpha selective agonists. European Journal of Pharmacology *427*, 285-293.

Washington, I.M., and Van Hoosier, G. (2012). Clinical Biochemistry and Hematology. The Laboratory Rabbit, Guinea Pig, Hamster, and Other Rodents, 57-116.

Winkler, E.S., Bailey, A.L., Kafai, N.M., Nair, S., McCune, B.T., Yu, J., Fox, J.M., Chen, R.E., Earnest, J.T., Keeler, S.P., *et al.* (2020). SARS-CoV-2 infection of human ACE2-transgenic mice causes severe lung inflammation and impaired function. Nature Immunology *21*, 1327-1335.

Yinda, C.K., Port, J.R., Bushmaker, T., Owusu, I.O., Avanzato, V.A., Fischer, R.J., Schulz, J.E., Holbrook, M.G., Hebner, M.J., Rosenke, R., *et al.* (2020). K18-hACE2 mice develop respiratory disease resembling severe COVID-19. bioRxiv.

Zhong, J., Tang, J., Ye, C., and Dong, L. (2020). The immunology of COVID-19: is immune modulation an option for treatment? The Lancet Rheumatology *2*, e428-e436.

Figure titles and legend

Figure 1: High-fat and high-sugar diet induces metabolic changes characterized by increased juvenile weight gain and glucose tolerance. Male Syrian hamsters were fed either a regular or high-fat high-sugar diet *ad libitum* for 16 weeks. **A.** Relative weight gain in hamsters on each diet regimen, measured weekly. Graphs show median ± 95% CI, N = 35, ordinary two-way ANOVA, followed by Sidak's multiple comparisons test. **B.** Oral glucose tolerance test performed at 16 weeks. Graphs show median ± 95% CI, N = 30 (RD) / 29 (HFHS), ordinary two-way ANOVA, followed by Sidak's multiple comparisons test. **C.** Insulin response after application of oral glucose load as shown by insulin resistance index (fasting glucose level (mmol/L) x fasting insulin level (mIU/L)). Truncated violin plots depicting median, quartiles and individuals, N = 30 (RD) / 29 (HFHS), Mann-Whitney test. **D**. Adiposity index as measured by testicular fat pads/total body weight at 16 weeks. Truncated violin plots depicting median, quartiles and individuals, N = 5, Mann-Whitney test. **E.** Blood lipid ALT and cholesterol levels measured on a commercially available lipid panel on an automated blood chemistry analyzer. **F.** Serum aggregate lipids signal analyzed by liquid chromatography tandem mass spectrometry (LC-MS/MS) at 16 weeks of diet

691 regimen. Truncated violin plots depicting median, quartiles and individuals, N = 5(RD) / 4 (HFHS),
692 Mann-Whitney test. Abbreviations: RD = regular diet, HFHS = high-fat high-sugar, ALT = alanine
693 aminotransaminase. p-values are indicated were appropriate.

694
695 **Figure 2. High-fat and high-sugar diet induces liver damage and systemic hyperlipidemia.**
696 Male Syrian hamsters were fed either a regular or high-fat high-sugar diet *ad libitum* and 5 animals
697 from each group were sacrificed week 16 for analyses of liver tissue. **A.D.** Gross imaging of a
698 representative liver from one hamster on the RD and one hamster on the HFHS diet regimen.
699 **B.E.** 20x photomicrograph of H&E-stained slide. **C.F.** 400x photomicrograph of H&E-stained slide.
700 **G.** RNA was isolated for gene expression analyses from liver tissue at 16 weeks. Using Integrated
701 Pathway Analysis (Qiagen), significantly up-regulated canonical pathways were identified.
702 Graphs show pathways associated with cell recruitment, activation, and immunological
703 inflammation ($p > 0.05$, z-score < -2 or > 2). **H.** Integrated Pathway Analysis (Qiagen) was used
704 to depict the gene network associated with nonalcoholic steatohepatitis. Symbols refer to legend
705 below figure. Red: Gene upregulation in high-fat high-sugar animals as compared to regular diet
706 animals. Green: downregulation in comparison to regular diet.

707
708 **Figure 3: High-fat and high-sugar diet exasperated disease severity after SARS-COV-2**
709 **infection.** Male Syrian hamsters were fed either a regular or high-fat high-sugar diet *ad libitum*
710 for 16 weeks, then challenged with $8x10^4$ $TCID_{50}$ SARS-CoV-2. **A.** Survival after challenge for RD
711 (N = 10) and HFHS (N = 9) in the 14 and 21 DPI groups **B.** Relative weight loss in hamsters after
712 challenge. Left graph shows median ± 95% CI. Right graph shows area under the curve (AUC,
713 negative peaks only) between 1-14 DPI of surviving animals. Truncated violin plots depicting
714 median, quartiles and individuals, N = 10 (RD)/ 7 (HFHS), Mann-Whitney test. **C.** Lung function
715 analysis after challenge **D**. Pressure-volume loops at pre-challenge, 7, 14, and 21 DPI.
716 Abbreviations: RD = regular diet, HFHS = high-fat high-sugar, DPI = days post inoculation. p-
717 values are indicated were appropriate.

718
719 **Figure 4. High-fat and high-sugar diet is associated to increased pulmonary pathology and**
720 **decreased viral clearance.** Animals were euthanized at 7 DPI with SARS-CoV-2 in order to
721 compare lung pathology and viral titers. **A-J.** Gross and photomicrographic images of hamster
722 lungs taken at 7 DPI. **A, F.** Gross necropsy findings consisted of multifocal well-circumscribed
723 dark red foci throughout turgid lobes which failed to collapse. **B, G.** Dark red foci in the gross
724 images correlate with the consolidated foci adjacent to airways and scattered along the pleural
725 margin in the sub-gross images. HE, 1.4x. **C, H.** Foci of interstitial pneumonia adjacent to terminal
726 bronchioles and accompanying blood vessels. HE, 20x. **D, I.** Pneumonia consists of alveoli
727 containing neutrophils, eosinophils, alveolar and septal macrophages, fibrin, edema and septa
728 lined by hyperplastic type II pneumocytes, HE 400x. Syncytial cells are common (see inset, HE,
729 1000x). Pneumonic areas in the HFHS diet hamsters frequently had abundant intra–alveolar
730 edema (*) and organizing fibrin mixed with inflammatory cells. Note the vessel wall disrupted by
731 sub-endothelial leukocytes and cellular debris (←). **E, J.** anti-SARS-CoV-2 immunoreactivity in
732 the lungs from the regular diet hamsters is rare compared to the frequent pneumocyte
733 immunoreactivity in the lungs of the HFHS diet hamsters, IHC, 400x. **K.** Individual pathological
734 scores. **L.** Quantitative count of SARS-CoV-2 immunoreactivity by morphometric analysis.
735 Truncated violin plots depicting median, quartiles and individuals, N = 10 (RD) / 4 (HFHS), Mann-
736 Whitney test. **M.N.** Lung viral load measured by g and sgRNA. Truncated violin plots depicting
737 median, quartiles and individuals, N = 10 (RD) / 4 (HFHS), Mann-Whitney test. **O.** Infectious virus
738 measured by lung titration. Truncated violin plots depicting median, quartiles and individuals, N =
739 10 (RD) / 4 (HFHS), Mann-Whitney test. Dotted line = limit of detection. Abbreviations: g =
740 genomic, sg = subgenomic, DPI = days post inoculation, H&E = hematoxylin and eosin stain, IHC
741 = immunohistochemistry. p-values are indicated were appropriate.

742
743 **Figure 5. Immune infiltration and in the lung during acute-phase of infection and humoral**
744 **immunity is not significantly affected by high-fat high-sugar diet.** Animals were euthanized

745 at 0, 7 and 14 DPI and the presence of SARS-CoV-2 antigen, T-cells, B-cells and macrophages
746 investigated. **A, B.** Pre-challenge RD and HFHS diet hamster lungs. **G, H.** IBA1; **M, N.** CD3 and
747 **S, T.** Pax5. **C, D.** Lungs at 7 DPI. **I, J.** IBA1; **O, P.** CD3 and **U, V** Pax 5. **E, F.** Lungs at 14 DPI.
748 **K, L.** IBA1; **Q, R.** CD3 and **W, X.** Pax 5. **A-F** HE. All images 200x. Abbreviations: RD = regular
749 diet, HFHS = high-fat high-sugar, DPI = days post inoculation.
750
751 **Figure 6. Disease manifestation is accompanied by prolonged viral shedding, systemic**
752 **immune and metabolomic dysregulation after high-fat high-sugar diet.** Animals were
753 euthanized pre-challenge, at 7, 14, and 21 DPI with SARS-CoV-2 and serum and lung tissue
754 collected for immune and lipid mediator analyses. Oropharyngeal swabs were taken to assess
755 respiratory shedding **A.B.** Lung infiltration of T-cells (CD3) and macrophages (IBA1) was
756 quantified by morphometric analysis. Truncated violin plots depicting median, quartiles and
757 individuals, pre-challenge and 14 DPI: N = 2, 7 DPI: N = 10 (RD) / 4 (HFHS), ordinary two-way
758 ANOVA, followed by Turkey's multiple comparisons test. **C.** ELISA titers against spike protein of
759 SARS-CoV-2 (lineage A) in serum obtained pre-challenge, at 7, 14, and 21 DPI. Truncated violin
760 plots depicting median, quartiles and individuals, pre-challenge and 14 DPI: N = 5 (RD) / 4
761 (HFHS), 7 DPI: N = 10 (RD) / 4 (HFHS), 21 DPI: N = 5 (RD) / 3 (HFHS), ordinary two-way ANOVA,
762 followed by Sidak's multiple comparisons test. **D.** Virus neutralization titers against SARS-CoV-2
763 (lineage A) in serum obtained at 14 and 21 DPI. Truncated violin plots depicting median quartiles
764 and individuals, 14 DPI: N = 5 (RD) / 4 (HFHS), 21 DPI: N = 5 (RD) / 3 (HFHS), ordinary two-way
765 ANOVA, followed by Sidak's multiple comparisons test. **E.F**. Viral load in oropharyngeal swabs
766 measured in sgRNA copy number for RD and HFHS animals. Graphs show median, individual
767 animals and 95% CI (shaded area). Dotted line = peak shedding. **G.** Area under the curve (AUC)
768 analysis of virus shedding shown in E/F. Truncated violin plots depicting median quartiles and
769 individuals, 21 DPI: N = 5 (RD) / 3 (HFHS), Mann-Whitney test. **H.** Serum levels (pg/mL) of INF-
770 γ, TNFα-, IL-6 and IL-10 measured by ELISA from serum collected on 0, 7, 14, and 21 DPI.

771 Truncated violin plots depicting median quartiles and individuals, pre-challenge/14 and 21 DPI: N
772 = 5 (RD) / 4 (HFHS), 7 DPI: N = 10 (RD) / 4 (HFHS), ordinary two-way ANOVA, followed by
773 Sidak's multiple comparisons test. **I.** Lipid time-course heatmap: Changes in PUFA-containing
774 serum lipids associated with an active SARS-CoV-2 infection as measured by LC-MS/MS.
775 Autoscaled intensities are displayed for serum lipids species that were significantly changed
776 between 0 and 7 DPI in either regular diet or HFHS diet hamsters with a false discovery rate of
777 15 % equating to p = 0.0256, 0.0193 for RD and HFHS, respectively. *FA22:6 (HFHS p = 0.0374)
778 is displayed for comparison to clinical data despite not passing FDR filters. Abbreviations: TNF =
779 tumor necrosis factor, IFN = interferon, IL = interleukin, RD = regular diet, HFHS = high -fat high-
780 sugar, DPI = days post inoculation, sg = subgenomic, VN = virus neutralization. p-values are
781 indicated were appropriate.
782

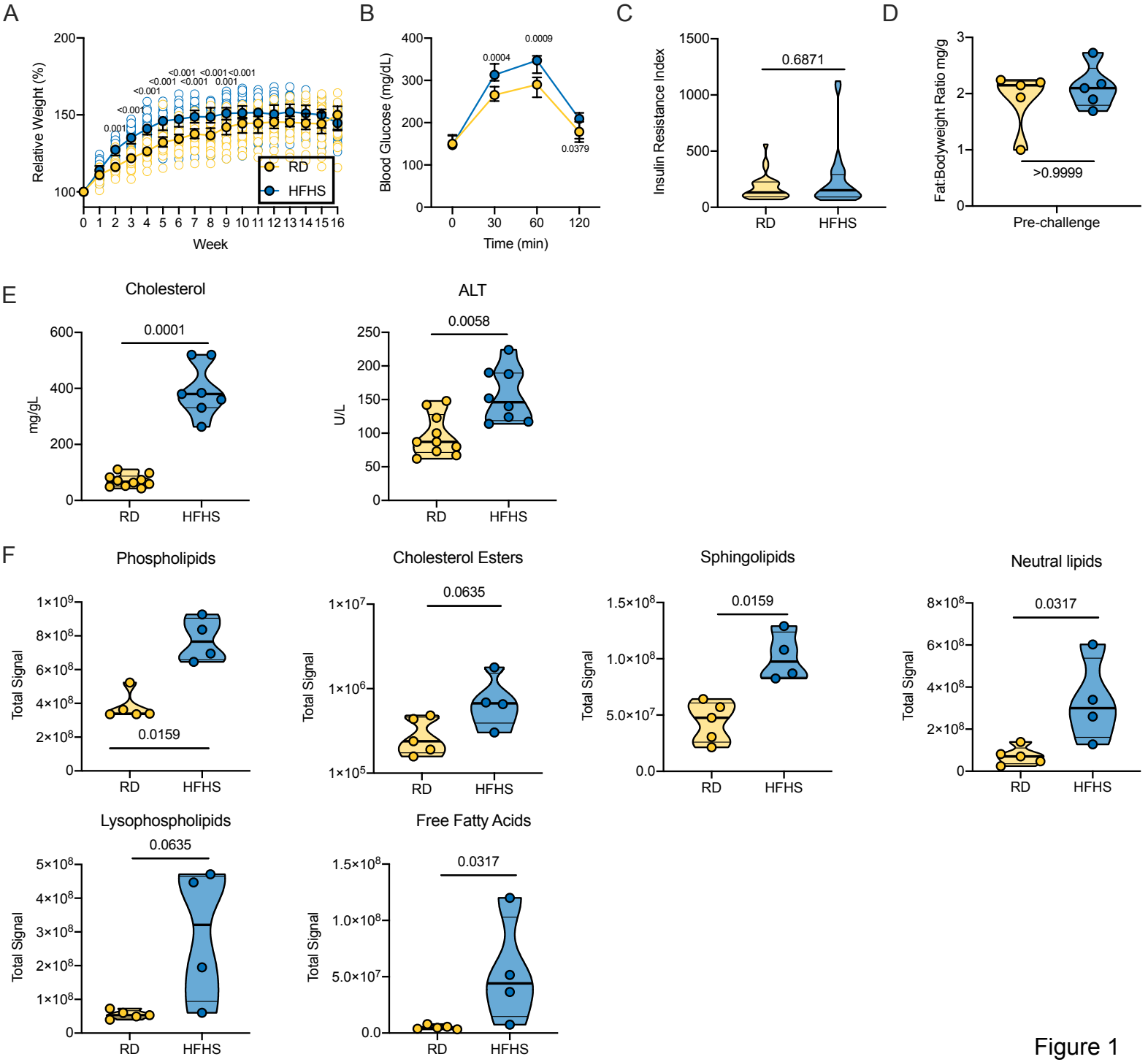
A
Relative Weight (%)
Week
RD
HFHS
B
Blood Glucose (mg/dL)
Time (min)
0.0004
0.0009
0.0379
C
Insulin Resistance Index
0.6871
RD
HFHS
D
Fat:Bodyweight Ratio mg/g
>0.9999
Pre-challenge
E
Cholesterol
mg/gL
0.0001
ALT
U/L
0.0058
F
Phospholipids
Total Signal
0.0159
Cholesterol Esters
0.0635
Sphingolipids
0.0159
Neutral lipids
0.0317
Lysophospholipids
0.0635
Free Fatty Acids
0.0317

Figure 1

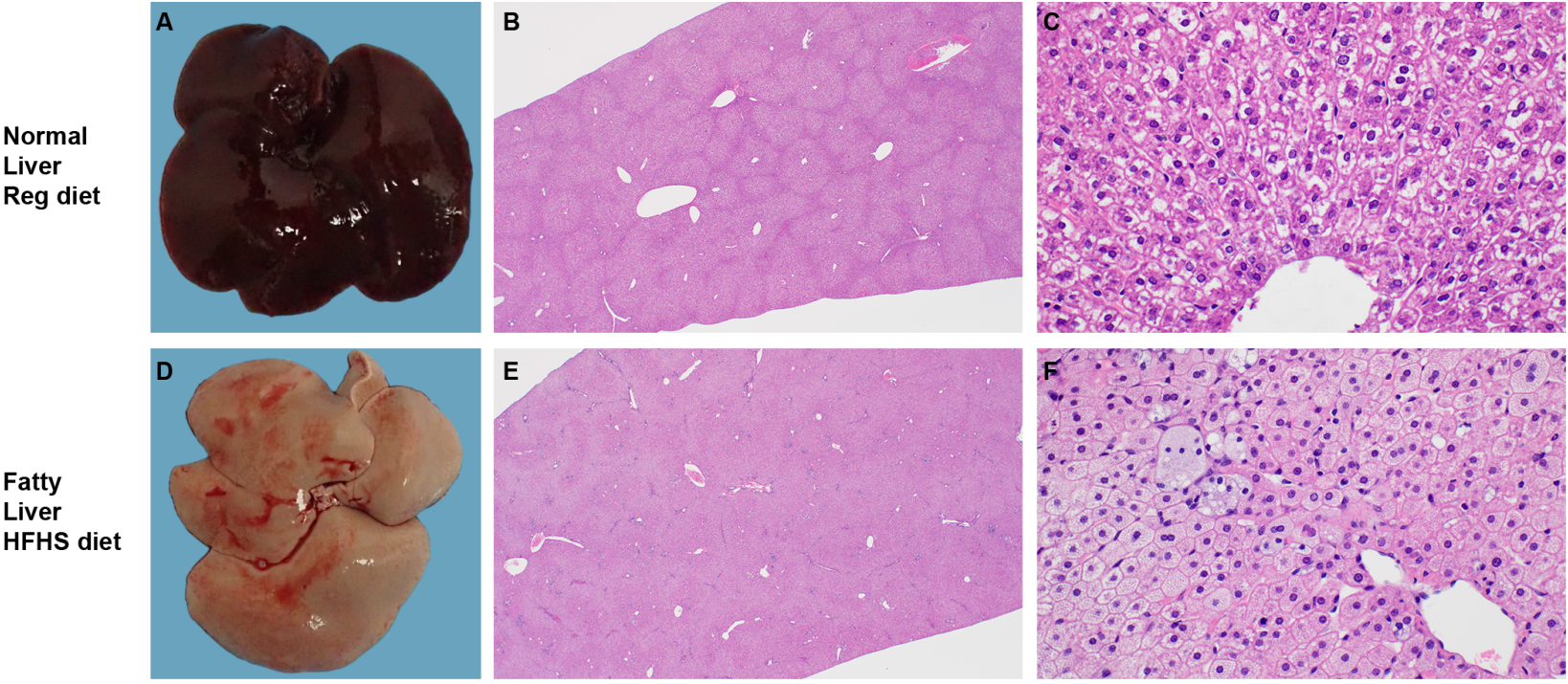
Normal
Liver
Reg diet
Fatty
Liver
HFHS diet
A
B
C
D
E
F

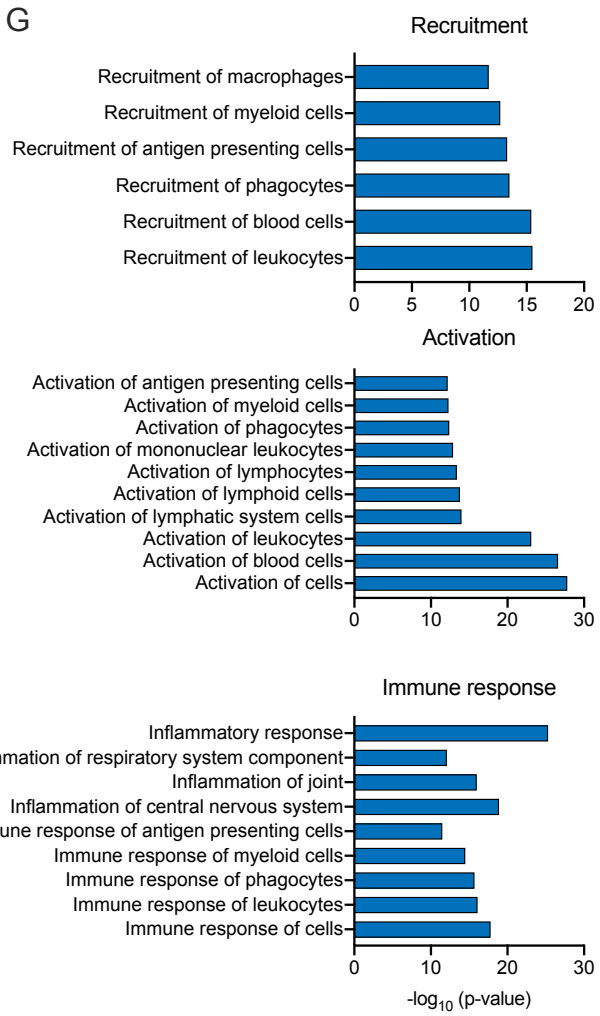
G
Recruitment
Recruitment of macrophages
Recruitment of myeloid cells
Recruitment of antigen presenting cells
Recruitment of phagocytes
Recruitment of blood cells
Recruitment of leukocytes
0
5
10
15
20
Activation
Activation of antigen presenting cells
Activation of myeloid cells
Activation of phagocytes
Activation of mononuclear leukocytes
Activation of lymphocytes
Activation of lymphoid cells
Activation of lymphatic system cells
Activation of leukocytes
Activation of blood cells
Activation of cells
0
10
20
30
Immune response
Inflammatory response
Inflammation of respiratory system component
Inflammation of joint
Inflammation of central nervous system
Immune response of antigen presenting cells
Immune response of myeloid cells
Immune response of phagocytes
Immune response of leukocytes
Immune response of cells
0
10
20
30
-log10 (p-value)

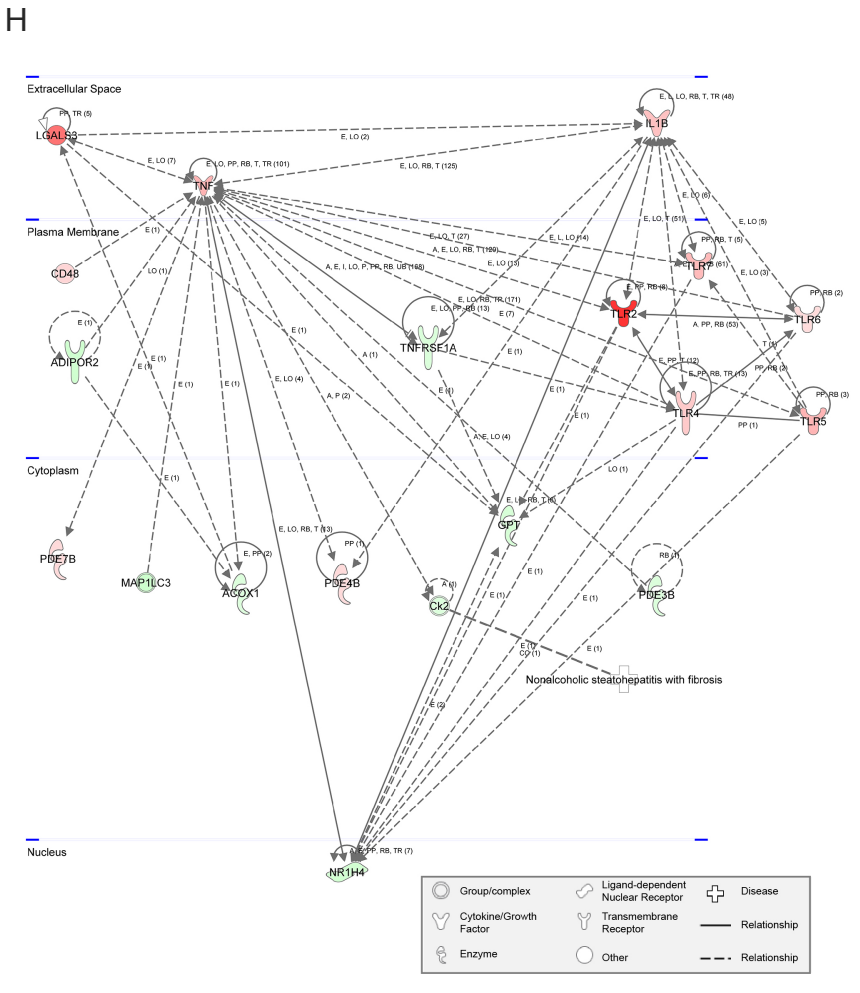
H
Extracellular Space
Plasma Membrane
Cytoplasm
Nucleus
LGALS9
IL1B
TNF
CD48
ADIPOR2
TNFRSF1A
TLR2
TLR4
TLR6
TLR5
GPT
PDE7B
MAP1LC3
ACOX1
PDE4B
Ck2
PDE3B
NR1H4
Nonalcoholic steatohepatitis with fibrosis
Group/complex
Cytokine/Growth Factor
Enzyme
Ligand-dependent Nuclear Receptor
Transmembrane Receptor
Other
Disease
Relationship
Relationship

Figure 2

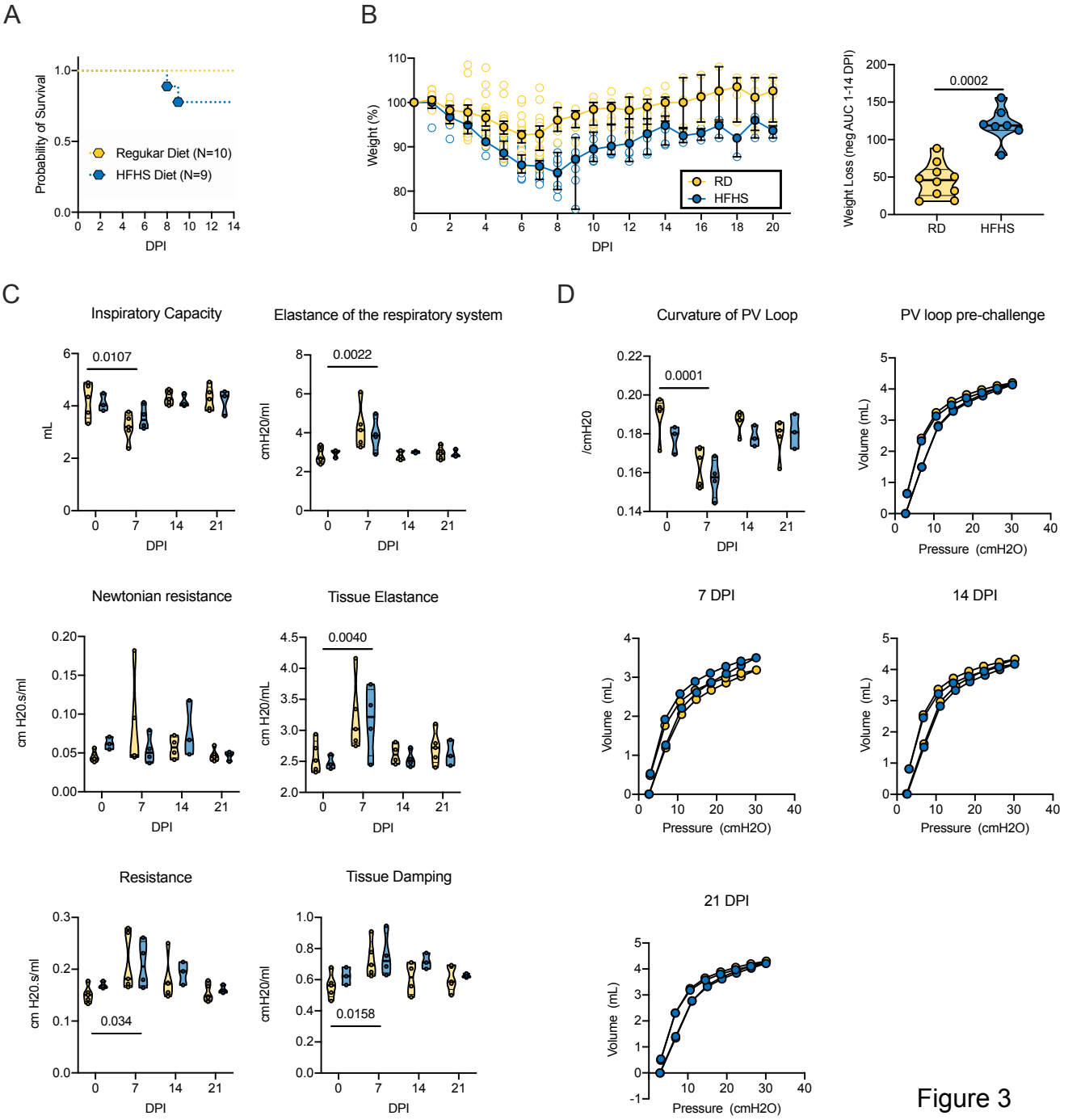
A
Probability of Survival
Regukar Diet (N=10)
HFHS Diet (N=9)
DPI
B
Weight (%)
RD
HFHS
DPI
Weight Loss (neg AUC 1-14 DPI)
0.0002
RD
HFHS
C
Inspiratory Capacity
0.0107
mL
DPI
Elastance of the respiratory system
0.0022
cmH20/ml
DPI
Newtonian resistance
cm H20.s/ml
DPI
Tissue Elastance
0.0040
cm H20/mL
DPI
Resistance
0.034
cm H20.s/ml
DPI
Tissue Damping
0.0158
cmH20/ml
DPI
D
Curvature of PV Loop
0.0001
/cmH20
DPI
PV loop pre-challenge
Volume (mL)
Pressure (cmH2O)
7 DPI
Volume (mL)
Pressure (cmH2O)
14 DPI
Volume (mL)
Pressure (cmH2O)
21 DPI
Volume (mL)
Pressure (cmH2O)

Figure 3

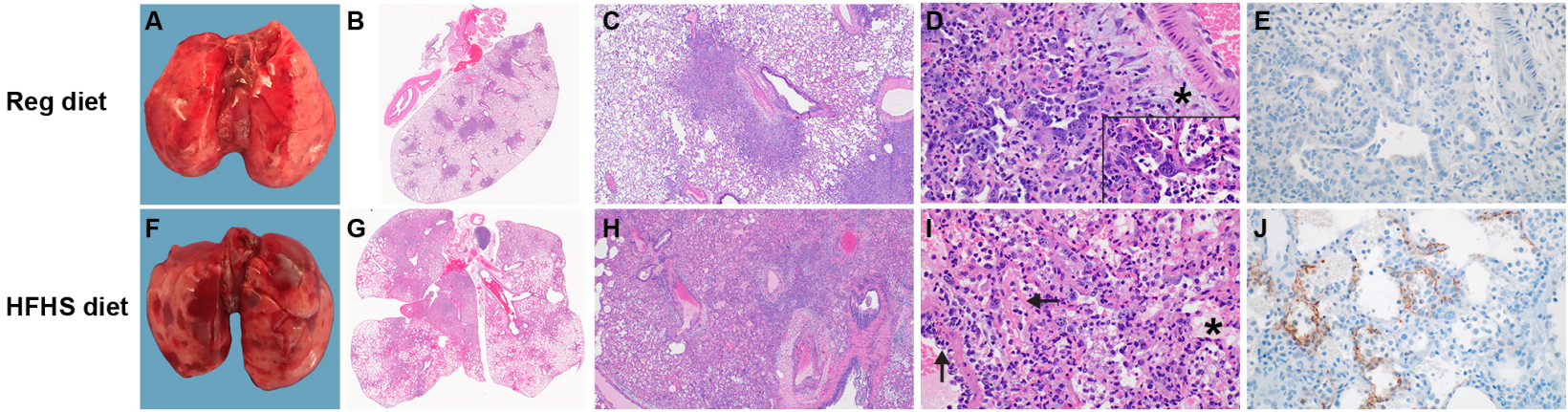

K

	RD 1	RD 2	RD 3	RD 4	RD 5	RD 6	RD 7	RD 8	RD 9	RD 10	HFHS 1	HFHS 2	HFHS 3	HFHS 4
Percentage affected	70	30	20	30	40	70	50	40	60	60	70	60	50	30
Interstitial Pneumonia	4	2	2	3	3	4	3	3	4	4	4	3	3	2
Syncytial Cell	1	1	1	1	1	1	1	1	1	1	1	1	1	1
Alveolar and bronchial exudate	3	2	2	2	2	3	3	3	3	3	4	4	4	3
Bronchiolar epithelial cell inflamm/necrosis	0	0	0	0	0	0	0	0	0	0	1	1	1	1
Perivascular leukocyte cuffing	0	0	0	0	0	0	0	0	0	0	0	0	0	0
vasculitis - neutrophilic	2	2	1	1	2	1	1	1	2	2	3	3	3	2
Type II pneumocyte hyperplasia	1	1	1	1	1	1	1	1	1	1	1	1	1	1
Hemorrhage, fibrin and or edema	3	2	2	1	1	4	3	0	4	4	4	3	3	3

0 = No lesions
1 = Minimal (1-10%)
2 = Mild (11-25%)
3 = Moderate (26-50%)
4 = Marked (51-75%)
5 = Severe (76-100%)

Figure 4

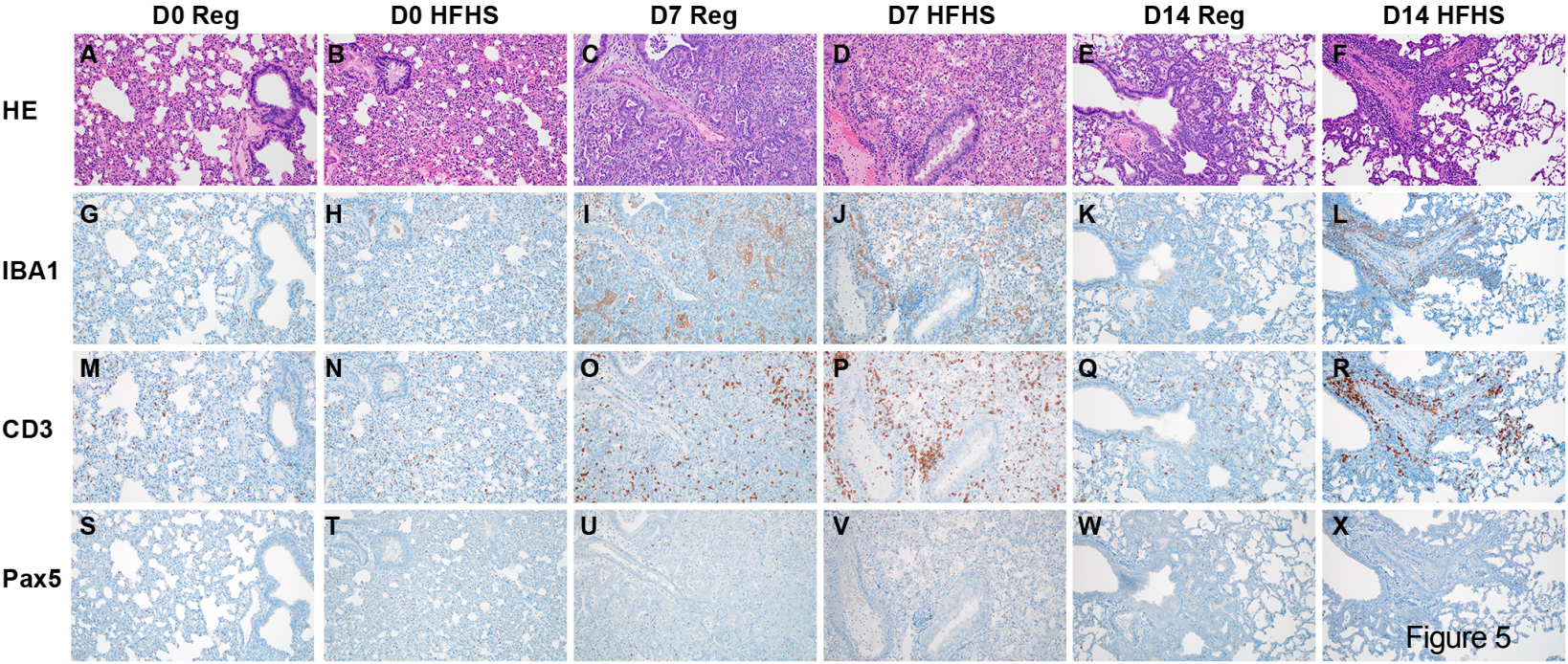
D0 Reg
D0 HFHS
D7 Reg
D7 HFHS
D14 Reg
D14 HFHS
HE
IBA1
CD3
Pax5
A
B
C
D
E
F
G
H
I
J
K
L
M
N
O
P
Q
R
S
T
U
V
W
X

Figure 5

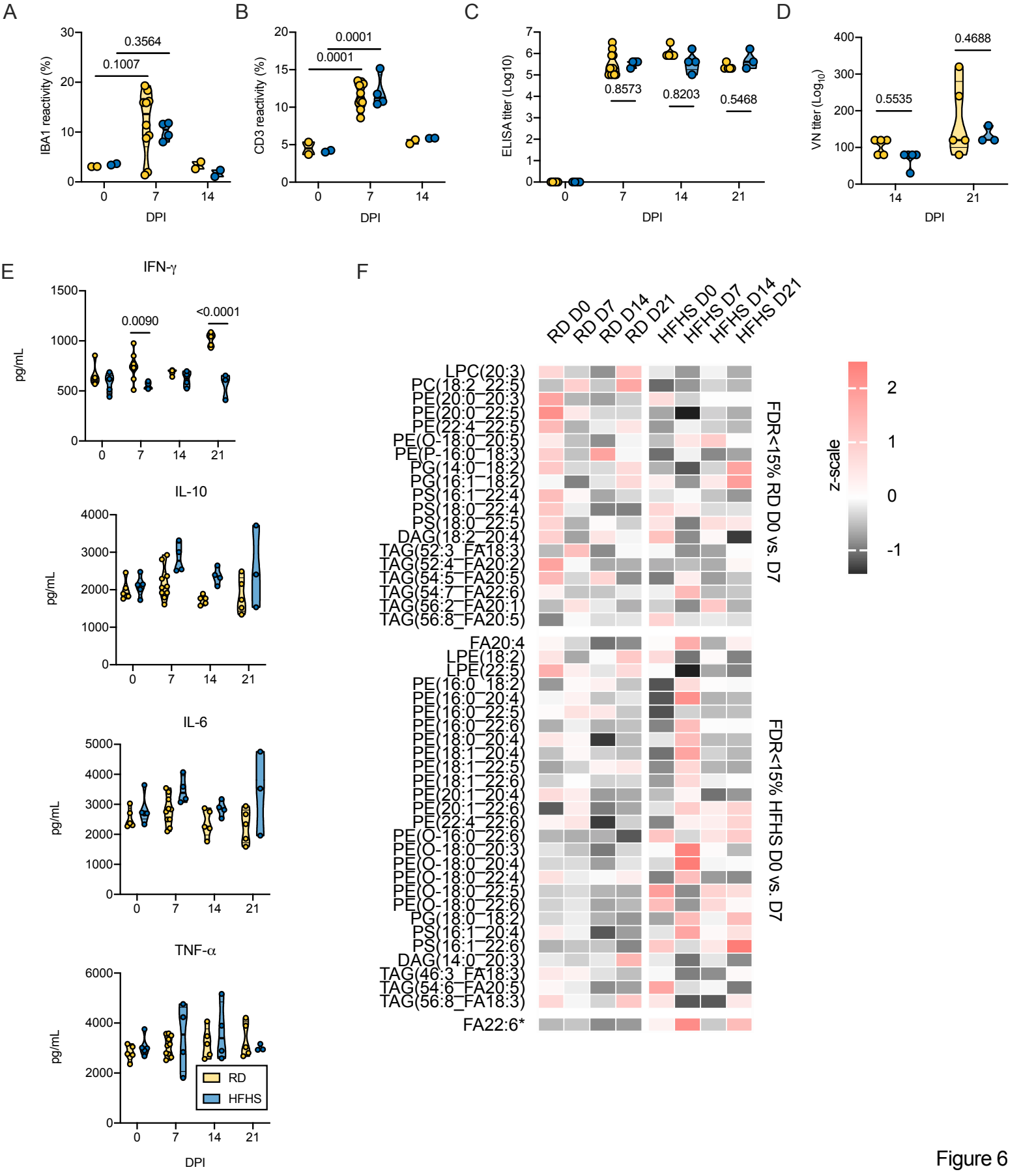
A
IBA1 reactivity (%)
0.1007
0.3564
DPI
B
CD3 reactivity (%)
0.0001
0.0001
DPI
C
ELISA titer (Log10)
0.8573
0.8203
0.5468
DPI
D
VN titer (Log10)
0.5535
0.4688
DPI
E
IFN-γ
pg/mL
0.0090
<0.0001
IL-10
pg/mL
IL-6
pg/mL
TNF-α
pg/mL
RD
HFHS
DPI
F
RD D0
RD D7
RD D14
RD D21
HFHS D0
HFHS D7
HFHS D14
HFHS D21
LPC(20:3)
PC(18:2_22:5)
PE(20:0_20:3)
PE(20:0_22:5)
PE(22:4_22:5)
PE(O-18:0_20:5)
PE(P-16:0_18:3)
PG(14:0_18:2)
PG(16:1_18:2)
PS(16:1_22:4)
PS(18:0_22:4)
PS(18:0_22:5)
DAG(18:2_20:4)
TAG(52:3_FA18:3)
TAG(52:4_FA20:2)
TAG(54:5_FA20:5)
TAG(54:7_FA22:6)
TAG(56:2_FA20:1)
TAG(56:8_FA20:5)
FDR<15% RD D0 vs. D7
FA20:4
LPE(18:2)
LPE(22:5)
PE(16:0_18:2)
PE(16:0_20:4)
PE(16:0_22:5)
PE(16:0_22:6)
PE(18:0_20:4)
PE(18:1_20:4)
PE(18:1_22:5)
PE(18:1_22:6)
PE(20:1_20:4)
PE(20:1_22:6)
PE(22:4_22:6)
PE(O-16:0_22:6)
PE(O-18:0_20:3)
PE(O-18:0_20:4)
PE(O-18:0_22:4)
PE(O-18:0_22:5)
PE(O-18:0_22:6)
PG(18:0_18:2)
PS(16:1_20:4)
PS(16:1_22:6)
DAG(14:0_20:3)
TAG(46:3_FA18:3)
TAG(54:6_FA20:5)
TAG(56:8_FA18:3)
FA22:6*
FDR<15% HFHS D0 vs. D7
z-score

Figure 6

Supplemental Material

Western diet increases COVID-19 disease severity in the Syrian hamster

Julia R. Port[1]*, Danielle R. Adney[1]*, Benjamin Schwarz[2], Jonathan E. Schulz[1], Daniel E. Sturdevant[3], Brian J. Smith[4], Victoria A. Avanzato[1], Myndi G. Holbrook[1], Jyothi N. Purushotham[1], Kaitlin A. Stromberg[2], Ian Leighton[2], Catharine M. Bosio[2], Carl Shaia[4], Vincent J. Munster[1]#

1. Laboratory of Virology, National Institute of Allergy and Infectious Diseases, National Institutes of Health, Hamilton, MT, USA
2. Laboratory of Bacteriology, National Institute of Allergy and Infectious Diseases, National Institutes of Health, Hamilton, MT, USA
3. Genomics Unit, Research Technologies Branch, National Institute of Allergy and Infectious Diseases, National Institutes of Health, Hamilton, MT, USA
4. Rocky Mountain Veterinary Branch, Division of Intramural Research, National Institutes of Health, Hamilton, MT, USA

*These authors contributed equally

#Corresponding author: Vincent Munster, email: vincent.munster@nih.gov

Supplemental Table 1: Liver marker profile in serum of regular diet (RD) and high-fat high-sugar diet (HFHS) after 16 weeks. Quantitative determination of total cholesterol (CHOL), high-density lipoprotein cholesterol (HDL), triglycerides (TRIG), alanine aminotransferase (ALT), aspartate aminotransferase (AST), and glucose (GLU) in heparinized whole blood. From the CHOL, HDL and TRIG determinations, low-density lipoprotein cholesterol (LDL), very low-density lipoprotein cholesterol (VLDL), non-HDL cholesterol, and a total cholesterol/high-density lipoprotein cholesterol ratio (TC/H) was calculated. ~~ + could not be calculated, LIP = not detectable due to lipid interference.

Animal ID	Chol mg/dl	HDL mg/dl	Trig mg/dl	ALT U/L	AST U/L	GLU mg/dl	nHDLc mg/dl	TC/H	LDL mg/dl	VLDL mg/dl	LIP
HFHS.1	360	LIP	~~~	124	78	120	~~~	~~~	LIP	LIP	3
HFHS.2	>520	HEM	HEM	224	HEM	LIP	~~~	~~~	~~~	~~~	3
HFHS.3	~~~	HEM	~~~	140	HEM	LIP	~~~	~~~	~~~	~~~	3
HFHS.4	>520	HEM	HEM	190	HEM	LIP	~~~	~~~	~~~	~~~	3
HFHS.5	380	LIP	>500	117	82	114	~~~	~~~	LIP	LIP	3
HFHS.6	263	LIP	>500	152	86	110	~~~	~~~	LIP	LIP	3
HFHS.7	384	~~~	~~~	188	147	LIP	~~~	~~~	~~~	~~~	3
HFHS.8	331	LIP	>500	114	84	59	~~~	~~~	LIP	LIP	2
Regular.1	83	49	212	62	76	113	34c	1.7c	0	42c	1
Regular.2	52	31	168	100	152	151	21c	1.7c	0	34c	0
Regular.3	98	68	248	67	79	72	30c	1.4c	0	50c	0
Regular.4	111	92	252	87	87	79	19c	1.2c	~~~	50c	1
Regular.5	74	43	184	73	96	98	31c	1.7c	0	37c	1
Regular.6	59	32	201	87	113	119	27c	1.8c	0	40c	1
Regular.7	43	23	204	148	127	101	20c	1.8c	~~~	41c	0
Regular.8	71	42	198	80	88	85	29c	1.7c	0	40c	0
Regular.9	64	46	232	142	157	88	18c	1.4c	~~~	46c	0
Regular.10	49	28	251	123	166	99	21c	1.7c	~~~	50c	0

Supplemental Table 2: Up-and down-regulated pathways in livers pre-challenge organized by disease and function.

Diseases or Functions Annotation	p-value	Predicted Activation State	Activation z-score	# Molecules
Development of genitourinary system	2.07E-11	Increased	2.114	160
Internalization of cells	1.99E-11	Increased	5.333	63
Abnormal bone density	1.99E-11	Decreased	-2.297	50
Phagocytosis of blood cells	1.89E-11	Increased	4.815	52
Adhesion of lymphocytes	1.54E-11	Increased	3.747	34
Interaction of T lymphocytes	1.36E-11	Increased	3.906	39
Adhesion of lymphatic system cells	1.33E-11	Increased	3.839	35
Cell movement of macrophages	1.32E-11	Increased	4.236	65
Adhesion of tumor cell lines	9.66E-12	Increased	2.42	68
Pancreatobiliary tumor	9.07E-12	Increased	2.146	402
Size of body	9.03E-12	Increased	2.966	126
Cell cycle progression	8.08E-12	Increased	2.341	171
Binding of T lymphocytes	7.98E-12	Increased	3.521	37
Interaction of lymphocytes	5.70E-12	Increased	3.973	45
Pancreatic lesion	5.57E-12	Increased	2.114	358
Migration of neutrophils	5.56E-12	Increased	3.941	38
Response of myeloid leukocytes	5.43E-12	Increased	2.565	34
Chemotaxis of neutrophils	5.10E-12	Increased	2.328	42
Migration of granulocytes	4.82E-12	Increased	3.2	43
Cell-cell contact	4.15E-12	Increased	2.864	136
Development of head	3.98E-12	Increased	3.325	164
Quantity of metal ion	3.75E-12	Increased	2.912	85
Aggregation of blood platelets	3.23E-12	Increased	3.084	49
Immune response of antigen presenting cells	3.23E-12	Increased	3.968	49
Binding of lymphatic system cells	2.58E-12	Increased	3.801	45
Transmigration of leukocytes	2.57E-12	Increased	2.603	42
Binding of lymphocytes	2.47E-12	Increased	3.619	43
Transport of molecule	2.41E-12	Increased	2.741	246
Malignant connective or soft tissue neoplasm	2.36E-12	Increased	2.079	203
Response of antigen presenting cells	1.93E-12	Increased	4.049	52
Recruitment of macrophages	1.92E-12	Increased	2.61	33

Engulfment of cells	1.87E-12	Increased	4.959	99
Phagocytosis	1.52E-12	Increased	5.163	81
Homing of neutrophils	1.47E-12	Increased	2.328	43
Phagocytosis of cells	1.45E-12	Increased	5.586	75
Binding of endothelial cells	1.13E-12	Increased	2.496	49
Transmigration of cells	1.13E-12	Increased	2.844	49
Cell movement of cancer cells	8.81E-13	Increased	2.68	41
Interaction of endothelial cells	8.80E-13	Increased	2.389	50
Cellular infiltration by myeloid cells	8.74E-13	Increased	2.023	72
Inflammation of respiratory system component	7.19E-13	Increased	2.017	105
Binding of lymphoid cells	7.09E-13	Increased	3.713	44
Activation of antigen presenting cells	6.15E-13	Increased	3.438	70
Homeostasis of blood cells	5.80E-13	Increased	3.757	111
Activation of myeloid cells	4.67E-13	Increased	3.734	74
Degranulation of phagocytes	4.12E-13	Increased	3.533	90
Activation of phagocytes	3.71E-13	Increased	3.826	79
Engulfment of myeloid cells	3.71E-13	Increased	4.655	47
Degranulation of myeloid cells	3.58E-13	Increased	3.647	91
Synthesis of reactive oxygen species	2.88E-13	Increased	4.241	99
Homeostasis of leukocytes	2.75E-13	Increased	3.757	110
Malignant neoplasm of retroperitoneum	2.37E-13	Increased	2.021	419
Quantity of Ca2+	2.14E-13	Increased	2.613	82
Engulfment of leukocytes	2.00E-13	Increased	4.233	51
Recruitment of myeloid cells	1.80E-13	Increased	4.402	64
T cell development	1.58E-13	Increased	3.822	104
Degranulation of leukocytes	1.56E-13	Increased	3.4	95
Upper gastrointestinal tract tumor	1.49E-13	Increased	2.236	581
Invasion of cells	1.48E-13	Increased	4.617	184
Engulfment of phagocytes	1.43E-13	Increased	4.266	49
Cell movement of tumor cell lines	1.37E-13	Increased	4.127	185
Metabolism of reactive oxygen species	1.34E-13	Increased	4.381	104
Growth of connective tissue	1.31E-13	Increased	2.459	123
Amyloidosis	1.30E-13	Decreased	-2.433	116
Activation of mononuclear leukocytes	1.19E-13	Increased	3.257	95

Upper gastrointestinal tract cancer	1.13E-13	Increased	2	580
Lymphopoiesis	9.10E-14	Increased	3.693	123
Adhesion of mononuclear leukocytes	7.27E-14	Increased	3.616	42
Quantity of immunoglobulin	6.65E-14	Increased	3.038	63
Production of antibody	6.01E-14	Increased	3.204	66
Cell viability	5.81E-14	Increased	4.969	235
Phagocytosis of phagocytes	4.62E-14	Increased	4.14	46
Phagocytosis of leukocytes	4.60E-14	Increased	4.229	47
Recruitment of antigen presenting cells	4.55E-14	Increased	3.038	38
Phagocytosis of myeloid cells	3.83E-14	Increased	4.396	46
Activation of lymphocytes	3.64E-14	Increased	3.171	93
Cell movement of T lymphocytes	3.42E-14	Increased	3.59	63
Recruitment of phagocytes	3.01E-14	Increased	4.827	62
Cell survival	1.69E-14	Increased	4.795	247
Activation of lymphoid cells	1.50E-14	Increased	3.25	94
Migration of myeloid cells	1.43E-14	Increased	3.972	54
Production of protein	1.43E-14	Increased	3.73	70
Quantity of B lymphocytes	1.29E-14	Increased	2.549	81
Activation of lymphatic system cells	1.09E-14	Increased	3.088	95
Metastasis	1.03E-14	Increased	3.523	181
Interaction of mononuclear leukocytes	9.60E-15	Increased	3.685	55
Growth of epithelial tissue	7.66E-15	Increased	2.312	135
Quantity of T lymphocytes	7.33E-15	Increased	4.155	111
T cell homeostasis	7.05E-15	Increased	3.667	109
Hematopoiesis of mononuclear leukocytes	6.16E-15	Increased	3.759	132
Migration of antigen presenting cells	4.15E-15	Increased	3.735	51
Immediate hypersensitivity	4.06E-15	Increased	2.362	77
Response of myeloid cells	3.82E-15	Increased	4.283	60
Immune response of myeloid cells	2.85E-15	Increased	4.069	56
Non-colon gastrointestinal cancer	2.59E-15	Increased	2	612
Aggregation of cells	2.51E-15	Increased	3.773	77
Extraadrenal retroperitoneal tumor	2.51E-15	Increased	2.58	463
Chemotaxis of myeloid cells	2.36E-15	Increased	3.493	70
Leukopoiesis	2.22E-15	Increased	4.158	149

Aggregation of blood cells	1.69E-15	Increased	3.56	62
Differentiation of mononuclear leukocytes	1.67E-15	Increased	3.796	134
Hereditary connective tissue disorder	1.43E-15	Decreased	-3.259	128
Binding of mononuclear leukocytes	1.33E-15	Increased	3.331	54
Advanced malignant tumor	8.44E-16	Increased	3.434	197
Connective tissue tumor	7.45E-16	Increased	2.495	222
Advanced stage tumor	5.25E-16	Increased	3.434	198
Chemotaxis of phagocytes	4.47E-16	Increased	3.987	73
Recruitment of blood cells	4.05E-16	Increased	4.395	79
Connective or soft tissue tumor	3.53E-16	Increased	2.525	249
Degranulation of cells	3.26E-16	Increased	3.573	115
Recruitment of leukocytes	2.92E-16	Increased	4.208	78
Chemotaxis of leukocytes	2.63E-16	Increased	4.146	84
Immune response of phagocytes	2.22E-16	Increased	4.017	62
Growth of tumor	2.05E-16	Increased	4.005	179
Degranulation	1.09E-16	Increased	3.507	117
Inflammation of joint	1.07E-16	Increased	3.397	178
Response of phagocytes	9.69E-17	Increased	4.268	66
Chemotaxis of blood cells	9.45E-17	Increased	4.147	85
Recruitment of cells	8.37E-17	Increased	4.692	85
T cell migration	7.55E-17	Increased	4.271	73
Immune response of leukocytes	7.50E-17	Increased	4.727	80
Hypersensitive reaction	6.65E-17	Increased	3.831	97
Vasculogenesis	5.92E-17	Increased	3.35	158
Angiogenesis	5.56E-17	Increased	4.04	184
Development of vasculature	4.93E-17	Increased	3.955	198
Binding of tumor cell lines	4.04E-17	Increased	2.518	93
Homing of leukocytes	3.51E-17	Increased	4.4	89
Cell movement of antigen presenting cells	2.39E-17	Increased	4.024	91
Binding of myeloid cells	2.30E-17	Increased	3.053	60
Cellular homeostasis	2.19E-17	Increased	4.676	269
Experimental autoimmune encephalomyelitis	1.82E-17	Increased	3.58	86
Homing of blood cells	1.80E-17	Increased	4.405	90
Interaction of tumor cell lines	1.57E-17	Increased	2.283	96
Microtubule dynamics	6.51E-18	Increased	3.927	216
Cell movement of granulocytes	5.63E-18	Increased	3.593	93

Cell movement of lymphatic system cells	2.90E-18	Increased	4.135	101
Organization of cytoplasm	2.90E-18	Increased	4.437	262
Cell movement of neutrophils	2.55E-18	Increased	3.635	83
Encephalitis	2.39E-18	Increased	2.541	95
Immune response of cells	1.57E-18	Increased	4.854	130
Cell movement of lymphocytes	1.14E-18	Increased	4.249	100
Allergy	5.20E-19	Increased	3.26	98
Rheumatic Disease	4.02E-19	Increased	3.322	223
Organismal death	3.96E-19	Decreased	-4.3	362
Morbidity or mortality	2.66E-19	Decreased	-4.307	366
Cell proliferation of T lymphocytes	2.10E-19	Increased	2.415	127
Development of body trunk	1.36E-19	Increased	3.651	215
Binding of professional phagocytic cells	1.35E-19	Increased	2.925	61
Inflammation of central nervous system	1.33E-19	Increased	2.333	102
Invasive tumor	1.09E-19	Increased	3.538	224
Migration of lymphatic system cells	8.48E-20	Increased	4.544	95
Lymphocyte migration	5.97E-20	Increased	4.62	94
Organization of cytoskeleton	5.36E-20	Increased	4.437	249
Chemotaxis	4.82E-20	Increased	4.815	123
Migration of mononuclear leukocytes	3.71E-20	Increased	4.931	99
Proliferation of lymphocytes	3.65E-20	Increased	3.292	150
Proliferation of immune cells	3.58E-20	Increased	3.303	158
Proliferation of lymphatic system cells	3.30E-20	Increased	3.653	159
Homing of cells	2.85E-20	Increased	4.933	128
Interaction of phagocytes	2.61E-20	Increased	3.318	64
Quantity of lymphatic system cells	1.12E-20	Increased	4.27	161
Proliferation of blood cells	8.94E-21	Increased	2.84	172
Migration of phagocytes	7.21E-21	Increased	5.059	82
Proliferation of mononuclear leukocytes	3.68E-21	Increased	3.384	154
Quantity of lymphocytes	1.41E-21	Increased	4.164	155
Cell movement of mononuclear leukocytes	7.82E-22	Increased	4.793	119
Quantity of lymphoid cells	7.71E-22	Increased	4.267	156
Cell movement of myeloid cells	9.41E-23	Increased	5.148	136
Atherosclerosis	5.83E-23	Increased	2.673	111

Arteriosclerosis	5.55E-23	Increased	2.673	112
Cancer of cells	5.08E-23	Increased	2.324	684
Occlusion of artery	8.44E-24	Increased	2.291	124
Activation of leukocytes	7.41E-24	Increased	3.906	152
Quantity of mononuclear leukocytes	3.21E-24	Increased	4.23	166
Development of digestive organ tumor	2.85E-24	Increased	2.223	805
Occlusion of blood vessel	1.78E-24	Increased	2.439	127
Cell movement of phagocytes	2.32E-25	Increased	5.16	143
Vaso-occlusion	1.80E-25	Increased	2.762	130
Inflammatory response	5.12E-26	Increased	4.721	179
Neoplasia of cells	4.32E-26	Increased	3.343	764
Nervous system neoplasm	1.09E-26	Increased	2.631	863
Binding of leukocytes	6.17E-27	Increased	4.377	107
Adhesion of immune cells	3.52E-27	Increased	4.659	102
Activation of blood cells	2.67E-27	Increased	4.18	171
Binding of blood cells	1.99E-28	Increased	4.151	117
Activation of cells	1.77E-28	Increased	4.235	212
Adhesion of blood cells	1.50E-29	Increased	4.576	110
Cell movement of leukocytes	2.69E-31	Increased	5.68	193
Leukocyte migration	2.22E-31	Increased	6.163	217
Quantity of cells	2.80E-32	Increased	4.371	346
Migration of cells	2.28E-33	Increased	5.915	387
Quantity of leukocytes	8.59E-34	Increased	3.627	215
Quantity of blood cells	1.14E-34	Increased	3.879	234
Cell movement	1.12E-34	Increased	6.237	422
Digestive organ tumor	2.14E-45	Increased	2.245	1243
Intraabdominal organ tumor	1.16E-50	Increased	2.485	1285
Cancer	3.98E-60	Increased	3.984	1378
Solid tumor	1.91E-61	Increased	2.377	1380
Malignant solid tumor	6.41E-62	Increased	2.227	1377
Non-melanoma solid tumor	2.74E-65	Increased	2.163	1366

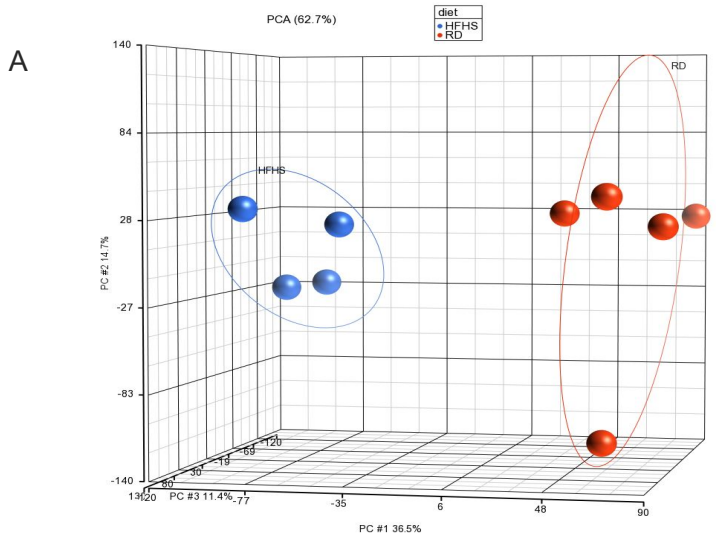

Supplemental Figure 1: A. RNA was isolated for gene expression analyses from liver tissue at 16 weeks and principal component analysis performed. Colors refer to legend on top. Abbreviations: RD = regular diet, HFHS = high-fat high-sugar, PC = principal component.

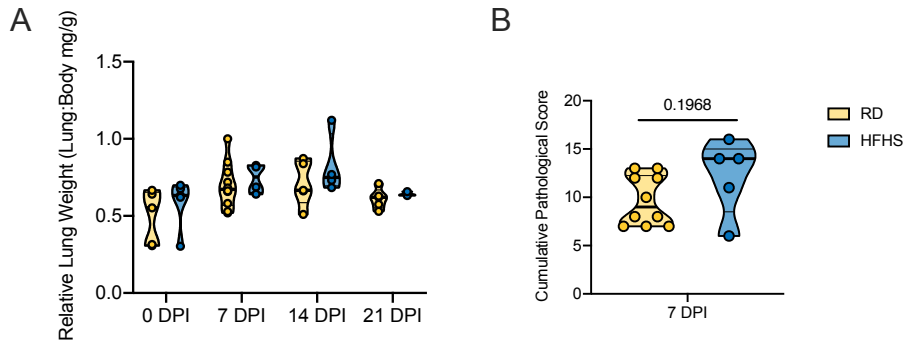

Supplemental Figure 2: Male Syrian hamsters were fed either a regular or high-fat high-sugar *diet ad libitum* for 16 weeks, then challenged with $8x10^4$ $TCID_{50}$ SARS-CoV-2. Animals were euthanized pre-challenge (0 DPI), at 7, 14 and 21 DPI. **A.** Lung weights. Truncated violin plots depicting median, quartiles, and individuals. **B.** Cumulative pathology score of lung tissues collected at 7 DPI. Truncated violin plots depicting median, quartiles and individuals, N = 10 (RD) / 4 (HFHS), Mann-Whitney test. Abbreviations: RD = regular diet, HFHS = high-fat high-sugar. p-values are indicated were appropriate.

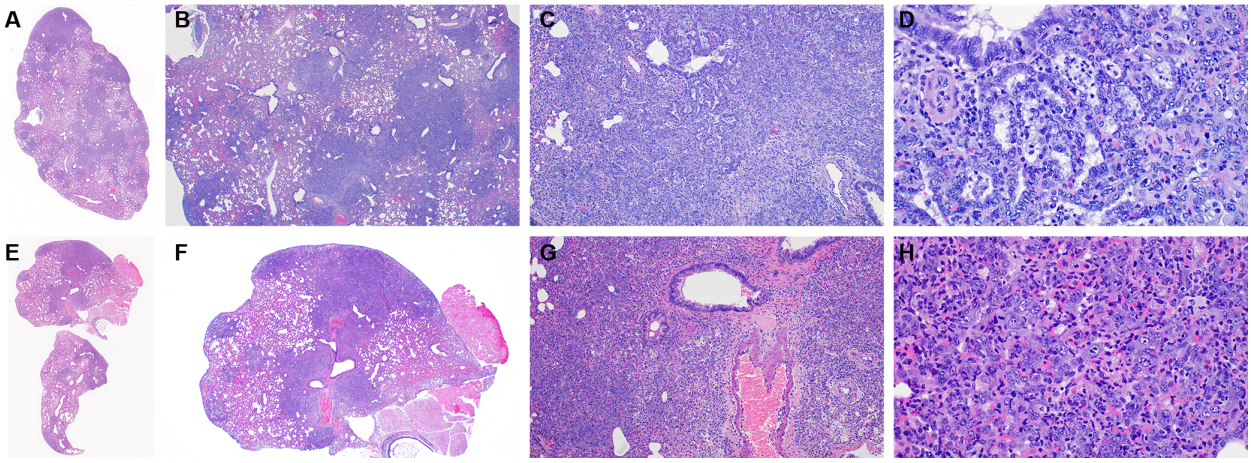

Supplemental Figure 3: Male Syrian hamsters were fed either a regular or high-fat high-sugar *diet ad libitum* for 16 weeks, then challenged with $8x10^4$ $TCID_{50}$ SARS-CoV-2. Animals were euthanized at day 8 and 9 due to increased weight loss. **A, E.** Dark, discreet foci identify areas of pneumonia; lighter areas indicate hemorrhage, edema, inflammation. HE, 1.4x. **B, F.** Although approximately 100% of the lobe is affected, only 50% contains discreet foci of interstitial pneumonia, HE, 20x. **C, D.** Examples of organized type II pneumocyte hyperplasia giving a honeycomb appearance. HE, 100x, 400x. **G, H.** Less well organized foci with more congestion, edema, and inflammation. HE, 100x, 400x. Of note, both appearances overlap and can be present in the same animal.

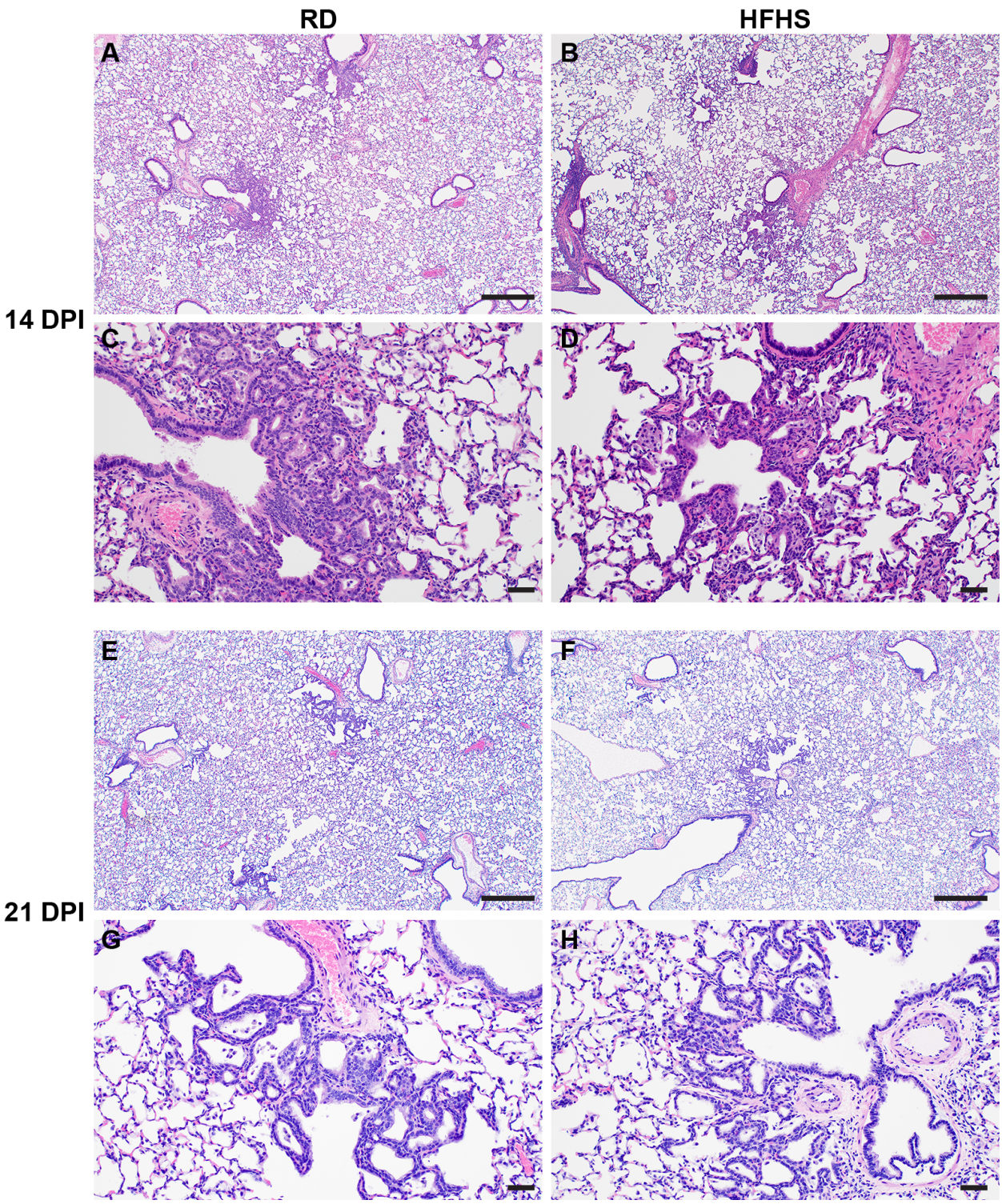

Supplemental Figure 4: Male Syrian hamsters were fed either a regular or high-fat high-sugar *diet ad libitum* for 16 weeks, then challenged with $8x10^4$ $TCID_{50}$ SARS-CoV-2. Lung tissues were collected 14 and 21 days post inoculation. **A, B**. 14 DPI, Lesions located at terminal bronchioles.

HE, 40x. **C, D**. 14 DPI, Thickened septa, alveolar bronchiolization and minimal inflammation. HE, 400x. **E, F**. 21 DPI, Lesions appear indistinguishable. HE, 40x. **G, H**. 21 DPI, Thickened septa and alveolar bronchiolization remain. HE, 400x. Abbreviations: Reg = regular diet, HFHS = high-fat high-sugar, DPI = days post inoculation.

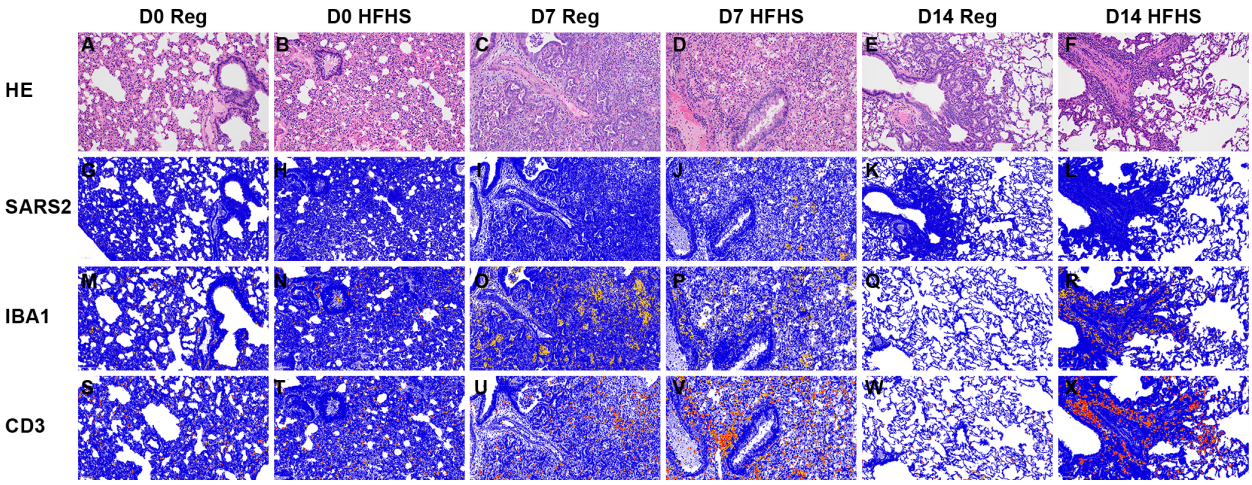

Supplemental Figure 5: Male Syrian hamsters were fed either a regular or high-fat high-sugar *diet ad libitum* for 16 weeks, then challenged with $8x10^4$ $TCID_{50}$ SARS-CoV-2. Animals were euthanized pre-challenge (0 DPI), 7 and 14 days post inoculation. Serial images of lungs. **A-F**. Pre-challenge lungs appear normal, 7 DPI lungs are pneumonic, and 14 DPI lungs appear to be resolving. HE, 200x. **G-L.** Positive pixel image of IHC staining against N protein of SARS-CoV-2. Note the positive pixels at 7 DPI in the HFHS image, 200x. **M-P.** Positive pixel image of IHC staining against IBA1. Note the increase in positive pixels at 7 and 14 DPI for both the RD and HFHS samples, 200x. **Q-X.** Positive pixel image of IHC staining against CD3, Note the increase in positive pixels at 7 and 14 DPI for both the RD and HFHS samples, 200x. Positive pixel = orange. Abbreviations: Reg = regular diet, HFHS = high-fat high-sugar, DPI = days post inoculation.